Finite element modeling of non-rigid origami

Parametric study on bistable origami using the finite element method

T. Smit

P&E report number 2831

Technische Universiteit Delft

Delft University of Technology

Challenge the future

Finite element modeling of non-rigid origami

Parametric study on bistable origami using the finite element method

by

T. Smit

in partial fulfillment of the requirements for the degree of

Master of Science
in Mechanical Engineering

at the Delft University of Technology,
to be defended publicly on Thursday July 13, 2017 at 09:00 AM.

Supervisor:	Dr. ir. A. M. Aragón
Thesis committee:	Prof. dr. ir. F. van Keulen Dr. ir. A. M. Aragón Dr. ir. F. Alijani

An electronic version of this thesis is available at `http://repository.tudelft.nl/`.

Delft
University of
Technology

Abstract

Origami has become a source of inspiration in engineering for structural design and the creation of mechanical metamaterials. In the often used analytic geometric and energy methods, it is difficult to incorporate deformation of the faces in non-rigid origami. However, deformation of the faces can play a significant role in their mechanical behaviour. This thesis aims to investigate and improve the design of non-rigid origami structures by using the Finite Element Method (FEM), which is well suited to model all deformations of these structures.

In collaboration with the Bertoldi Group at Harvard University, FEM is applied on the new bistable non-rigid origami structure called the Star bellow. The suitable building blocks of the FEM approach, are finite rotation shell elements to model the faces of the structure, torsional spring elements to model the crease lines, and a Newton-Raphson arc-length control solution procedure. In addition to the numerical analysis, experimental work is performed. A parametric study, FEM simulations, and physical load tests of prototypes, are performed to understand the mechanical properties of the Star bellow structure and to improve its bistable behaviour. In addition, the Star bellow structure was considered as a unit cell and tessellated into a 1D-array to create a Star bellow metamaterial. Simulations and physical load tests were performed to investigate the influence of the tessellation on the bistable properties of the metamaterial.

A design improvement was successfully proposed with a decrease of the minimum force value of 0.11 [N]. The tessellated Star bellow metamaterial into a 1D-array is feasible and keeps its bistable properties, although the bistability is reduced compared to a non-tessellated, single Star bellow structure.

The application of FEM to study the Star bellow structure enhances the design process of the Star bellow. It has been shown that a parametric study using FEM is a way to gain understanding of the structure's mechanical properties. Furthermore, a design change of the Star bellow was proposed which improved its bistable properties. It is also found that the results of the FEM simulations, for the force values, did not match the results of the physical load tests for various reasons. To improve this, another load testing setup and a more advanced implementation of the torsional spring elements to model the crease lines is advised.

Preface

First of all, I would like to thank my family in supporting me on my path through several schools and universities. It has been a long path, but I have always enjoyed it whether that was 'de Meerpaal' or Harvard. I also would like to thank Jimmy, with whom I studied in the past seven years, for his friendship and support.

During my thesis project I have learned a lot on Finite Element Methods (FEM), programming and many other things. During the thesis work, I more and more realized that students, including myself, get distracted quickly by fancy, colorful plots of FEM results. Not realizing that the real understanding is gained by analyzing simple problems in detail. During the implementation work of the shell elements I jumped into difficult test problems too quickly. Every time Professor Fred van Keulen forced me to do a step back and understand the real mechanics involved in the problem at hand. Therefore, I would like to thank him for his patience and advise. Furthermore, I would like to thank my supervisor Dr. Alejandro Aragón for his advise on programming and writing.

In this master thesis project I got the opportunity to join the Bertoldi group at Harvard University for three months. I would like to thank Professor Katia Bertoldi for giving me the opportunity. Furthermore, I would like to thank Dr. Ahmad Rafsanjani for supervising me during my stay.

Last but not least, the colleagues from the master student office. I would like to thank Bart, Rahul, Mahesh, Michael with whom I worked together on the development of hybrida .

T. Smit
Delft, July 2017

Contents

1 Introduction **1**
1.1 Analysis methods for origami structures . . . 2
1.2 Research goal . . . 3
1.3 Star bellow bistable origami structure . . . 4
1.4 Bistable origami . . . 4
1.5 Outline . . . 6

2 Finite Element Analysis of the Star bellow **7**
2.1 Mathematical model . . . 7
2.2 FEM approach for modeling the Star bellow . . . 8
2.3 Verification of the FEM approach . . . 8
2.4 Manufacturing and testing of the Star bellow . . . 10
2.5 Analysis and results of the Single Star bellow . . . 13
  2.5.1 Parametric study . . . 13
  2.5.2 Physical load testing of Single Star bellow prototype . . . 15
  2.5.3 FEM simulation of the Single Star bellow prototype . . . 16
  2.5.4 Design improvements and comparison . . . 18
2.6 Analysis and results of the Double Star bellow . . . 18
  2.6.1 Extended parametric study for the Double Star bellow . . . 18
  2.6.2 Physical load testing of Double Star bellow . . . 18
  2.6.3 FEM simulations of Double Star bellow . . . 19
2.7 Conclusions . . . 21
2.8 Outlook . . . 22

3 Reflection **23**
3.1 Process . . . 23
3.2 Time line . . . 24
3.3 Challenges . . . 24
3.4 Contributions . . . 25

A Additional parametric study results **27**

B Additional FEM simulations **29**

C An assumed stress hybrid beam finite element formulation **31**

D A constant moment plate bending element **37**

E Consistent finite rotation shell elements **49**

F Hinge connection element **61**

G Periodic boundary conditions for finite rotation shell elements **63**

Bibliography **65**

1

Introduction

The ancient art of paper folding, currently referred to as Origami, emerged around the 14th century [1]. The art of Japanese origin can be used to create a 3D structure by using a flat sheet of paper only. An example of origami is the Miuri-ori sheet shown in Figure 1.1.a. Inspired by the classical idea of origami, scientists and artists developed other types of origami structures and started using other materials than paper. One example is the new type kirigami, shown in Figure 1.1.b. In kirigami, in addition to folds, cuts can be used to increase the design freedom and broaden the applicability [2]. Origami became also a source of inspiration for mathematicians, engineers, and physicists for the development of new structural designs and materials. The inspirational role combined with the ease of manufacturing and testing of origami structures, has made origami a populated field of research in a broad range of sciences.

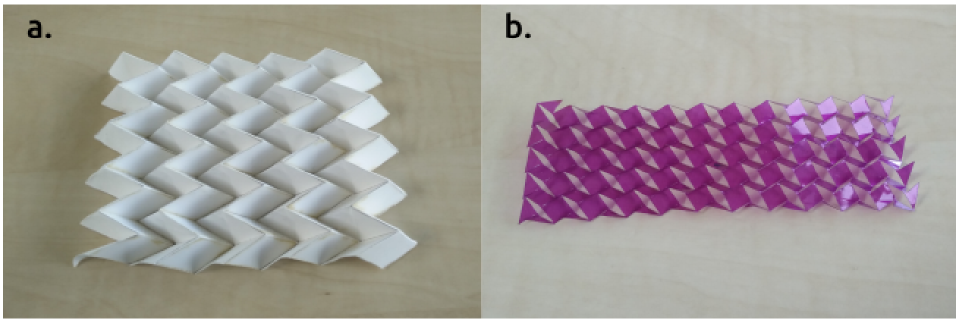

Figure 1.1: Figure a shows the Miuri-ori sheet
Figure b shows a kirigami structure [3].

Origami, in general, can be classified into two classes: rigid and non-rigid origami. This classification is of great importance as it influences the choice of suitable modeling methods. In rigid origami the structure's faces are assumed to be rigid links and the deformation only takes place along the crease lines [4, 5]. This assumption simplifies the mechanical calculations, but decreases the amount of possible folding motions per crease pattern. Rigid origami relates the most to classical origami, where no cutting or glueing could be done. Research with this classical approach is mainly the area of mathematicians and physicists. For example, one of their research topics is the flat-foldability of a crease pattern. A crease pattern is flat-foldable if it can be unfolded into a flat sheet without bending or crumpling of the faces [6]. In non-rigid origami the faces can deform, which increases the number of feasible crease patterns that have a folding motion [7]. In this class the rules are less strict and the research field is more populated by engineers, who design functional structures inspired by origami. This field of research is called engineering origami and focuses on exploiting structural instabilities of origami structures to create exotic mechanical behaviour. The advantage is that complex non-linear mechanical behaviour, like bistability, is created using linear elastic materials and low cost manufacturing techniques. To support the use of both origami classes in engineering applications like structural design or the development of a mechanical metamaterial, analytical and computational analysis methods to study the mechanical behaviour of origami structures are required.

The successful application of origami in structural design has already been demonstrated in several projects. An origami inspired structure could, for example, be transported compactly and then deployed to full size when used. This was shown by Zirbel *et al.* [8], where a deployable solar array was designed to be used in space applications. Origami has also shown to improve the structural design of airbags [9], deployable shelters [10], and energy absorbers [11]. Furthermore, origami-based design is applied to medical devices like stents [12], self-folding structures [13, 14], and compliant mechanisms [15–17]. Finally, origami has been a source of inspiration in architecture [18]. These examples emphasize the wide possibilities of origami in design.

Origami is, however, also adopted in the design of new materials, especially in mechanical metamaterials [5, 19]. Metamaterials are artificially constructed materials which can exhibit exotic mechanical properties. Furthermore, mechanical properties can be tuned by changing geometric parameters to accomplish behaviour which is not often found in nature [20–22]. These materials are created by tessellating a unit-cell in a periodic way and they realize their special mechanical properties due to their structural configuration and not solely to their material composition [23, 24]. Origami based mechanical metamaterials can demonstrate exotic mechanical behaviour like auxetic behaviour (negative Poisson's ratio) [3], multi-stability [25], mechanical hysteresis [20], and energy dissipation [26].

1.1. Analysis methods for origami structures

The continuously increasing interest of origami in engineering applications demands suitable computational methods to perform mechanical analyses. Currently, several methods are used to study the mechanical behaviour of origami. The most popular are the analytical geometric and energy methods. Another procedure to study the mechanical behaviour of origami is the Finite Element Method (FEM).

In the analytic procedures, mechanical properties like Poisson's ratio and strain energy curves can be obtained by formulating pattern-specific equations. In these equations, the motion of the structure is expressed as a function of one or two geometric variables and the mechanical properties can be derived from these equations analytically. This is illustrated by Hanna *et al.* [27, 28], who studied a bistable rigid origami structure named Waterbomb using an energy method to calculate the energy landscape and a virtual work analysis to obtain the force-displacement curve. Furthermore, Brunck *et al.* [29] demonstrated the geometric and energy methods for the mechanical analysis of the Miuri-ori sheet and the Waterbomb base. These methods are computationally efficient and can be applied to simulations involving large displacements and rotations. However, these analytic methods normally cannot take deformations into account of the faces of the origami structure, but only the deformation in the crease lines is modeled. For that reason, the application of these methods is normally restricted to rigid origami structures. Furthermore, a disadvantage of these methods is that the equation for describing the motion of the structure is only applicable to a specific crease pattern [30]. Another crease pattern or change in the geometry of the crease pattern usually results in a new analytic equation to describe the motion of the structure. Recent development in analytic methods is done by Chen *et al.* [31], who present a model to incorporate thick panels into geometric methods.

A FEM approach to simulate origami structures was reported by Resch [32] and later by Schenk [33, 34]. Resch used plane stress triangular elements to model the faces. Schenk used a truss framework with bar elements along the crease lines and triangulation of the faces. These two approaches, based on FEM, are not able to capture the bending deformation in detail of the faces [33]. Especially for the modeling of non-rigid origami, it is important to capture the bending of the faces in the modeling process since this can influence the mechanical behaviour of structures significantly [33]. The use of FEM, and specifically shell elements, to model the faces of origami structures, is already reported by Kshad [35], Gilewski *et al.* [36], Gilsario *et al.* [37], and by several other authors who use FEM to verify the analytic method they use [27, 38]. The use of FEM enables the easy change of the geometry of the structure. Also, different outputs can be generated, like energy and force-displacement curves, and stress distributions. The disadvantage of applying FEM is the computational time, which can be large compared to analytic methods. A recent development in the modeling of origami using FEM was presented by Peraza Hernandez *et al.* [7], who applied FEM to model smooth (non-ideal) crease lines which possess a certain folding curvature.

The application of FEM to the modeling of non-rigid origami structures is expected to overcome the drawbacks of the analytical methods. The application of FEM might enhance the design process because the geometry of an origami structure can be changed easily between simulations. Therefore a parametric study, were simulations for several geometric and material parameter values are performed, might speedup the design process. A parametric study, were FEM is used, is also reported by Wonoto *et al.* [39] and Crivaro [40].

1.2. Research goal

Application of FEM to non-rigid origami structures is expected to contribute to designing non-rigid origami. The research goal of this thesis is to:

> Investigate and improve the design of non-rigid origami structures using the Finite Element Method.

In collaboration with the Bertoldi Group at Harvard University, a new non-rigid bistable origami structure called the Star bellow, see Figure 1.2, is analyzed. In addition to the numerical analysis, experimental work is performed, consisting of the manufacturing of prototypes and physical load tests. The non-rigid nature of the bistability makes the Star bellow an ideal project for the FEM approach that is being researched in this thesis. By applying FEM to the Star bellow in the form of a parametric study, we aim to understand the structure's mechanical properties. Furthermore, we aim to improve the Star bellow's bistable behaviour. By combining the gathered knowledge from the parametric study, the results of the Star bellow's FEM simulations, and the load tests, a design improvement can be proposed. Load tests are performed to check an improvement in bistable properties. Herewith we study the Star bellow as a unit cell. In addition, a Star bellow metamaterial is created by tessellating the Star bellow unit cell into a 1D array. The mechanical behaviour of the Star bellow metamaterial is studied by additional simulations, prototyping and physical load tests.

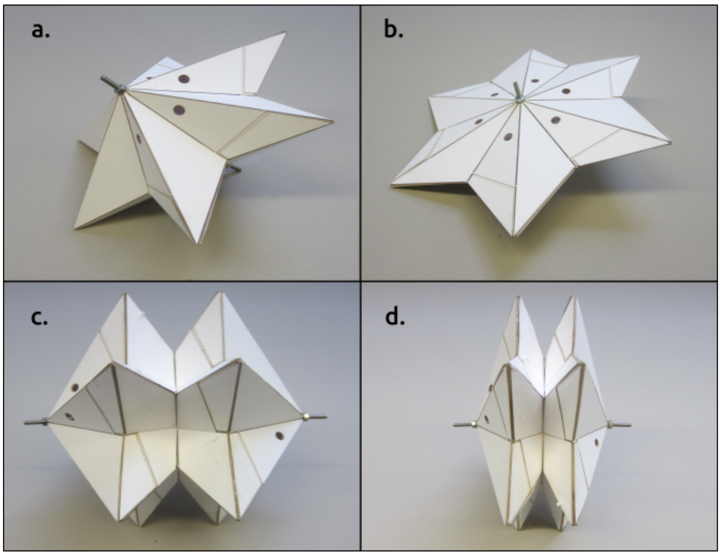

Figure 1.2: Star bellow bistable origami structures. Figure a shows the Single Star Bellow, deformed configuration and Figure b shows its undeformed configuration. Figure c shows the Double Star Bellow, deformed configuration and Figure d its undeformed configuration.

1.3. Star bellow bistable origami structure

The Star bellow consists of two star shaped panels which are connected by crease lines along the outer geometry. The star panels are built from 12 faces connected by mountain and valley creases. The long crease lines are mountain creases and the short crease lines are valley creases. The flat, initial configuration, is its first stable configuration. By pulling the centers of the stars outwards, the Star bellow will move toward its second stable configuration. The crease lines along the outer geometry remain planar (in the xy plane). Stretching and bending of the faces during the motion create the bistable behaviour. The length difference between the mountain and valley creases initiates deformation of the faces of the structure. At the limit point of the load, the deformation of the faces is at its maximum and from there faces start to relax. This relaxation results in snap-trough behaviour. Several geometric parameters play a role in the mechanical behaviour of the Star bellow. Figure 1.3.a shows a schematic with the length l of the long crease line, the angle of the tip of a face θ and the Cut-Back CB, which indicates the difference in length between the long and the short creases. The unit cell Star bellow will be denoted as the Single Star bellow and is shown in Figure 1.2.a and b.

To tessellate the Star bellow into a 1D-array we trim off the top of the Star bellow unit cell. The trim, denoted by Tr, is a percentage of the length of the long crease line l, see Figure 1.3.b. The trimmed sides are connected to create a 1D-array which is illustrated in Figure 1.3.c and d. Figure 1.2.c and d shows the tessellated Star bellow with two unit cells and a trim of $50\ \%$. The reason for this way of tessellating into a 1D-array is that, because of the trim, a cylindrical and inter-connected origami structure is created. Therefore, the 1D-array can be actuated by inflation. The tessellated Star bellow as discussed here will be denoted as the Double Star bellow.

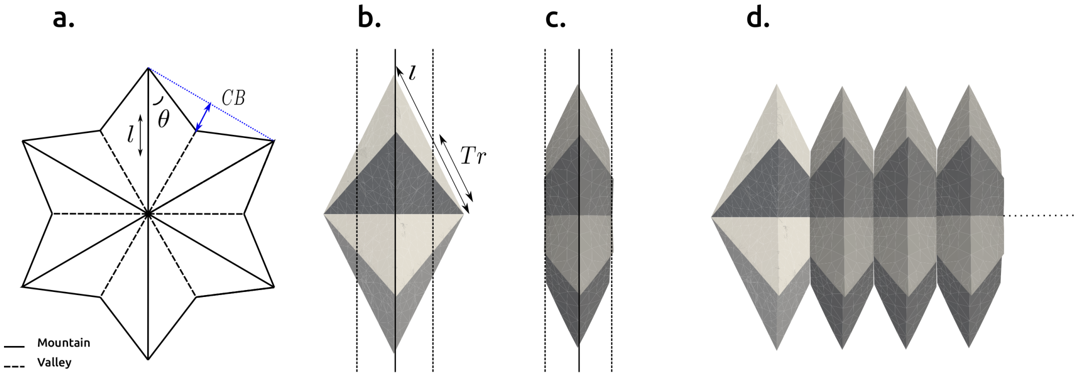

Figure 1.3: Figure a shows a schematic of the Single Star bellow, identified the length l of a mountain crease line and the Cut-Back CB. Figure b shows the definition of the trim Tr parameter. Figure c shows the trimmed Star bellow unit cell. Figure d shows the 1D-array tessellation to create a Star bellow metamaterial.

1.4. Bistable origami

The Single and Double Star bellows are both bistable. From an engineering point of view, bistable origami is interesting because it can add special structural behaviour to ordinary origami, broadening the range of applicability. Bistable structures exhibit two stable configurations [41]. Several groups of bistable origami structures are being researched. For example, there are bistable origami structures like the Waterbomb base [27, 28], the single vertex Metasheet [25], the Square twist [42], and the Multitransformable Leaf-Out [43]. Another group are origami structures where scientists use different existing origami patterns and configure them in cylindrical and extensible form [22, 38, 44, 45]. The additional advantage of the later group is that these can be actuated by pressurizing them [46, 47], like the Double Star bellow. Some structures of this group can also combine bistability and negative Poisson's ratio [48].

Bistability in origami structures can either originate from stretching and bending of the faces (non-rigid origami) or from spring like behaviour of the folds (rigid origami). An example of the latter is the already discussed, Waterbomb structure. Figure 1.4 shows both stable states for the Waterbomb. A structure reported in the literature, which is a bistable structure of the non-rigid class, is the cylindrical Kresling pattern [38, 45]. Figure 1.5 shows the states of the collapsed and extended configurations of the cylindrical Kresling pattern.

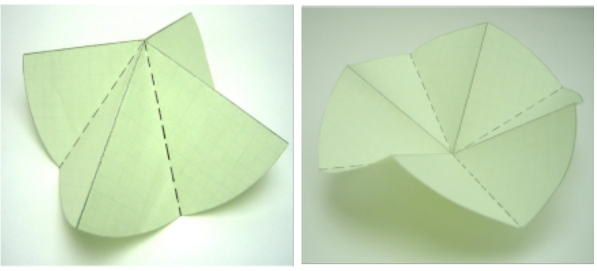

Figure 1.4: Waterbomb bistable origami structure [27].

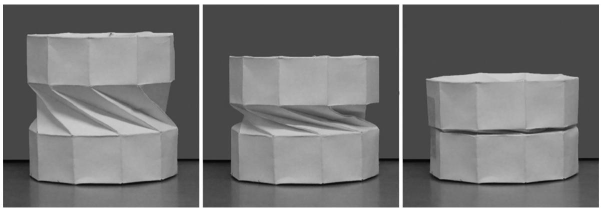

Figure 1.5: Configurations of the Cylindrical Kresling pattern. [45]

We can identify bistability by investigating the force-displacement curve and/or the total strain energy curve of the structure. For bistability we observe two load limit points and snap-trough behaviour in the force-displacement curve. The more extreme the maximum and minimum force values are, the more bistable the structure is. The corresponding energy landscape of the system should have two local minima separated by an unstable equilibrium at a local maxima. In ideal bistability, both local minima have the same value. Figure 1.6 a shows the characteristic curves for bistable behaviour. Metastability is a phenomenon where the total strain energy curve exhibit one local minimum with a higher energy value then the other. Therefore, the system can switch to the stable equilibrium by a small disturbance [49]. Figure 1.6 b shows the characteristic curve for metastability. Monostable systems can have load limit points and negative stiffness, but the force is never negative. This results in an ever increasing total strain energy curve without a second local minimum. These systems have only one energetic minimum and are therefore monostable. Figure 1.6 c shows the curve for a monostable system.

Mechanical hysteresis and energy absorption behaviour is often encountered in combination with bistability in origami structures [3, 17, 20, 42, 48, 50] Figure 1.7.a shows the energy absorption or energy trapping principle of bistable mechanisms. The absorbed energy is $E_{trapped} = E_{in} - E_{out}$ as was investigated by Shan [51]. From this statement, it follows that for ideal bistable and monostable mechanisms, no energy trapping can occur since E_{in} should be larger than E_{out}. Hysteresis in mechanical systems means that the loading path of a system is different from its unloading path. For cyclic loading cases the load path should form a loop. Since the loading and unloading paths are different, energy must be dissipated. The amount of energy which is dissipated is given by the area between the loading and unloading curves. Figure 1.7.b presents a typical force-displacement curve for hysteresis. The dark area indicates the dissipated energy. Several explanations are given in the literature for this phenomenon. Mittemeijer [52] attribute it due to a viscoelastic strain component. During loading and unloading, the viscoelastic strain component lacks behind the elastic strain. This viscoelastic component causes the difference between the loading and the unloading path and is called damping or mechanical elastic hysteresis. The dissipated energy is produced by elastic deformation and is dissipated as heat.

In figure 1.7.c the energy landscape is plotted for several strain parameters. The total strain energy is plotted which is the sum of the bending strain, membrane strain, and folding stain energy. To support a proper mechanical analyses, the strain components can be plotted separately.

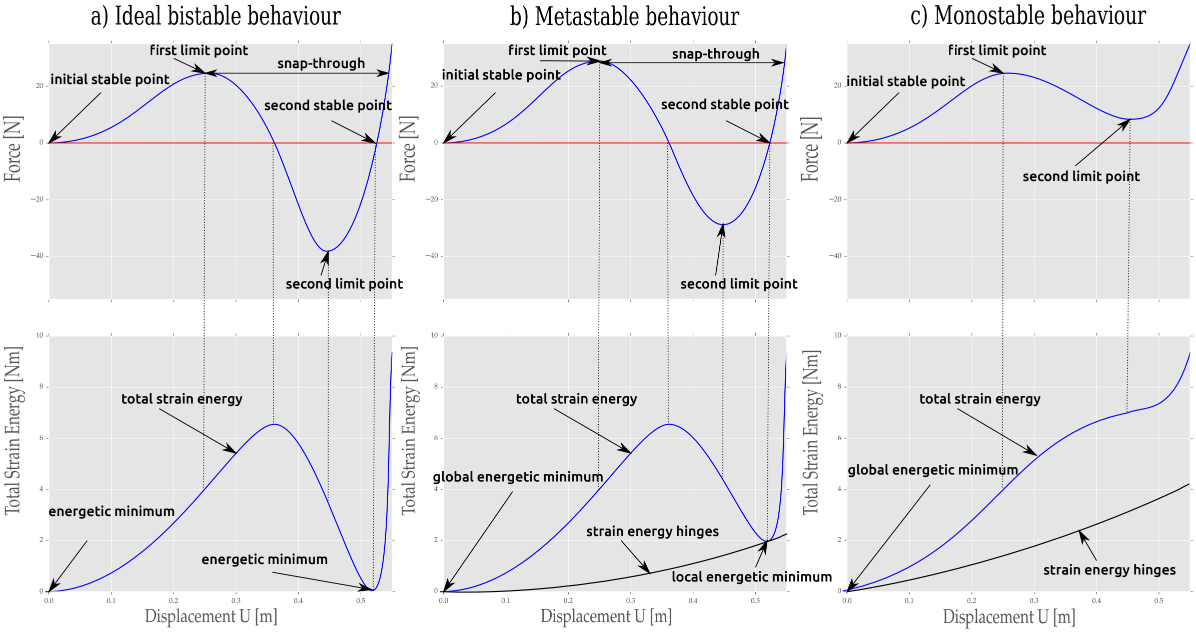

Figure 1.6: Bistable, metastable and monostable characteristic behaviour.

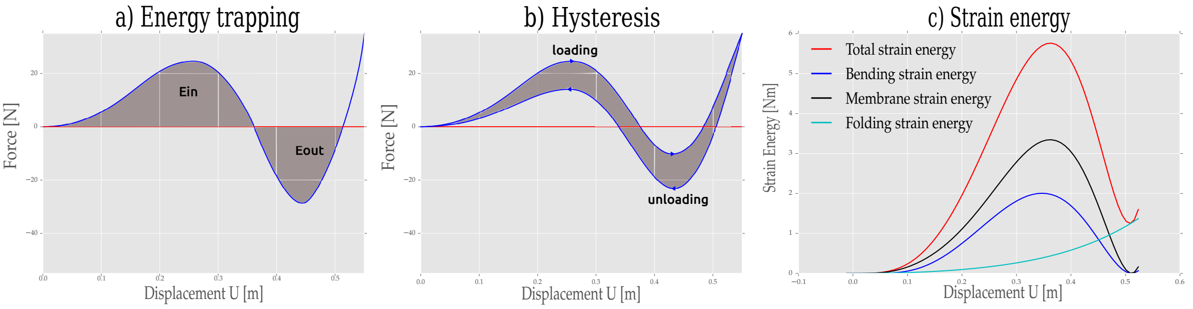

Figure 1.7: Energy trapping, hysteresis and strain energy.

1.5. Outline

Chapter 2 discusses the FEM approach to model non-rigid origami structures. The verification process is described, which includes a convergence study and a comparison of the FEM approach with the commercial code Abaqus. This is followed by a section on the Single Star Bellow which includes the parametric study, the load tests and FEM simulations. Then, a section is devoted to the Double Star bellow which includes additional FEM simulations and physical tests.

In chapter 3 a reflection on the process is given. This includes the line of thought, the learning process, and the contributions of the thesis work to the departments FEM code hybrida.

In the appendices, a detailed derivation will be given of the plate and shell elements which are used in this research. The derivation starts in appendix C with the demonstration of the assumed stress hybrid formulation for a beam finite element. Continuing this line, a constant moment plate bending element is derived in appendix D. Finally, the finite rotation shell element is discussed in appendix E.

2

Finite Element Analysis of the Star bellow

2.1. Mathematical model

Consider the symmetric origami structure shown in Figure 2.1, denoted by $\Omega \subset \Re^3$. The structure is composed by twelfth faces F_i, with each an area A_i. These faces are connected by crease lines C_i, with a length L_i. Because the thickness t of the faces is much smaller than the other dimensions, a plane stress assumption and a Kirchhoff-Love plate bending model would ideally describe the deformation of the faces. Furthermore, the in-plane deformation should also be taken into account. The internal virtual work becomes [53]

$$\delta W_{int} = \sum_{i=1}^{12} \int_{A_i} N^i_{\alpha\beta}\, \delta\gamma^i_{\alpha\beta} + M^i_{\alpha\beta}\, \delta\kappa^i_{\alpha\beta}\, dA_i + \sum_{i=1}^{12} \int_{L_i} k\, \phi^i\, \delta\phi^i\, ds.$$

with $(\alpha, \beta = 1, 2)$, N the membrane forces [N], and γ the in-plane strains, who are work conjugates. M denotes the bending moments [Nm], and κ the changes of curvature [1/m], who are also work conjugates. The torsional spring is defined on the crease lines. The k denotes the hinge stiffness [N/rad] and ϕ [rad] is defined as the rotational difference between the two faces. The external forces P acting on the Star bellow, shown in Figure 2.1 contribute to the external virtual work [53]

$$\delta W_{ext} = P\, \delta w$$

with P a force [N], who is work conjugated to the out of plane displacements w. Equilibrium can be obtained by $\delta W_{int} = \delta W_{ext}$. Finite displacements and rotations are observed during the motion of the Star bellow, leading to a non-linear system of equations. Therefore, a discretization and solution procedure suitable for finite displacements and rotations should be used.

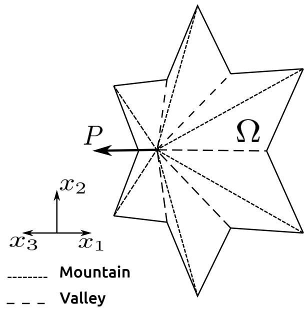

Figure 2.1: Schematic of the Star bellow indicating the load case and the mountain and valley creases.

2.2. FEM approach for modeling the Star bellow

The Star bellow structure is now discretized by triangular finite rotation shell elements with a consistent tangent operator, see Figure 2.2.a. The shell element is constructed by a combination of a constant strain triangle and a constant moment plate bending element formulated by an assumed stress hybrid formulation. The thin nature of sheet like material used for origami structures leads to the choice of using a plate element based on Kirchhoff assumptions. The membrane part of the element uses a total Lagrangian formulation and the bending part a finite rotation formulation. Therefore, the element is applicable to finite displacements and rotations analysis. The derivation of the shell element is described by van Keulen [53]. The derivation of the consistent tangent operator is described by Booij and van Keulen [54]. Appendix C demonstrates the assumed stress hybrid formulation. This formulation is used to formulate the constant moment plate bending element described in appendix D. Appendix E describes the derivation of the shell element in more detail.

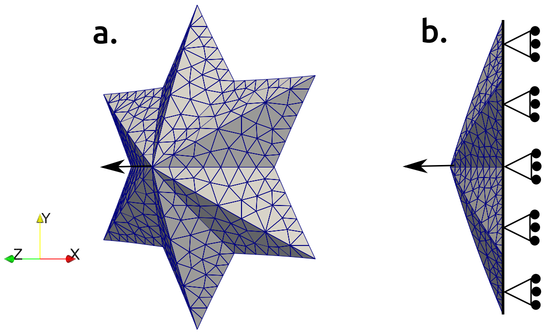

Figure 2.2: Figure a shows the discretization of the Star bellow model. Figure b shows the load case and boundary condition along edges in the symmetry plane.

Torsional spring elements are used to model the creases of the origami structure. The formulation of these elements is described by Donaldson [55], and Philip [56], and others. I implemented a torsional spring element in hybrida which can connect two shell elements by their sides along a crease line. The element is called a 'Hinge'. The Hinge element connects the translations of the shell elements combined corner nodes at the hinge locations and let the shell elements rotate relative to each other controlled by a torsional stiffness. Linear elastic torsion and zero hinge thickness are assumed. The torsional stiffness can be varied and can be interpreted as the resistance to folding of the crease line. The unit of the torsional stiffness input parameter is [N/rad]. Appendix F describes the derivation of the Hinge element in more detail.

Since snap-through behaviour is expected from bistable structures, a solution procedure which can deal with limit points in the load should be used. A Newton-Raphson with arc-length control is used, based on the unified solution approach discussed by Leon *et al.* [57] and Holtzer [58].

2.3. Verification of the FEM approach

The verification of the FEM simulation functionality as discussed in section 2.2 is divided in to three parts. The first part consist of the verification and testing of the building blocks of the FEM functionality individually and is described in the various appendices. The second part consists of a convergence check upon mesh refinement using an a posteriori goal-oriented error estimation. In the third part, the results from simulations of the Star bellow are compared, one is simulated using hybrida and one is simulated using the commercial FEM software Abaqus.

For the verification process, a model of the Single Star bellow is used with unit length l, Cut-Back CB of 24%, a Poisson's ratio of 0.3 and a Young's modulus of 1 [MPa]. The thickness choses to be 5% of the length l for the convergence study. Only one half of the Single Star bellow is modeled taking advantage of the symmetry of the structure. See Figure 2.2.b for the load and boundary conditions and the mesh.

A priori error estimation is not applicable to the symmetric Single Star bellow model because of its highly non-linear behaviour and the absence of an exact solution. Therefore, suggested by Gratsch *et al.* [59, 60], we adopt a goal-oriented error estimation. We select a scalar quantity who represent the entire state of the structure, which is the maximum value of the total strain energy E_{tot} as quantity of interest $Q = \max(E_{tot})$. The mesh size h is defined as the number of elements per crease line. Four refinement steps are used, 4, 8, 16 and 32 elements per crease, resulting in solutions denoted by Z. A reference solution Z_{ref} was obtained with a mesh of 64 elements per crease. The error in terms of the quantity of interest is

$$Q(e) = Q(Z) - Q(Z_{ref}).$$

The Relative Percentage Error (RPE) is calculated by normalizing the error in terms of the quantity of interest $Q(e)$

$$RPE = \frac{Q(e)}{Q(Z_{ref})}.$$

The rate of convergence c is calculated by

$$c = \frac{\log(Q(e)^{i}) - \log(Q(e)^{i+1})}{\log(h^{i}) - \log(h^{i+1})}.$$

The results of the convergence study are presented in Figure 2.3, where the force-displacement and energy curves are plotted for the mesh refinement study. Figure 2.4 shows the quantity of interest and the RPE versus the mesh size. These graphs show convergence of the quantity of interest and a quick decrease of the RPE. The quantity of interest convergence with a minimal rate of convergence of $c = 1.7$. Observing Figure 2.3 and 2.4 we see that for a mesh sizes of 16 elements per side the error is decreased to $6.5\,\%$ compared to the reference solution. For a mesh size of 32 the error is reduced to 1 percent of the reference solution. Taking to computational time in consideration we assume to obtain reasonably accurate results for mesh sizes between 16 and 32 elements per crease.

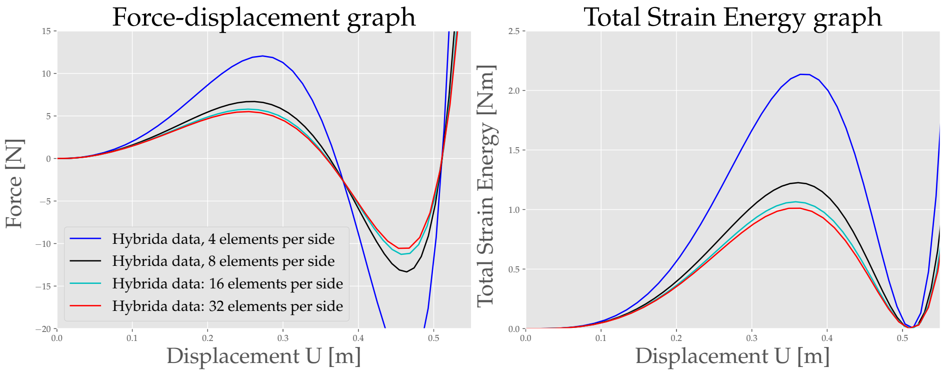

Figure 2.3: Resulting force-dispacement and energy curves for the mesh refinement study.

The second part of the verification process consists of a comparison of the symmetric Single Star bellow model simulated by hybrida and the commercial FEM software Abaqus. I recall that the hybrida shell element is derived by a Kirchhoff-Love (KL) formulation with constant bending and membrane stresses. The hybrida shell element is compared with two different Abaqus shell elements. The first is the $S3$ element, which is a well known and widely used shell element. The $S3$ is a triangular shell element based on Mindlin-Reissner (MR) plate bending theory. The second is the $STRI3$ triangular shell element based on Kirchhoff-Love theory. Both elements are facet elements and exhibit linear varying curvature and constant membrane strains [61]. The symmetric Single Star bellow model is used with three different thicknesses. This is done because the different element formulations can influence the obtained results and the magnitude of the influence is depending on the thickness.

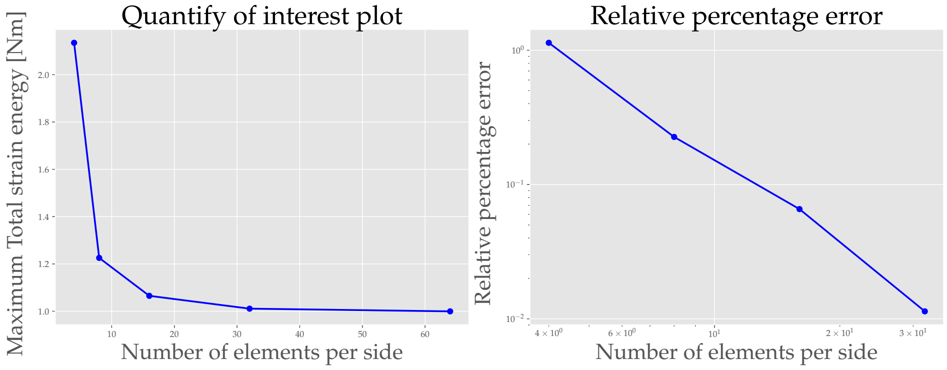

Figure 2.4: Convergence of the quantity of interest and the RPE for the mesh refinement study.

The thickness is chosen to be 2%, 5% and 10% of the length l. A mesh of 8 elements per crease is used. Furthermore, the crease lines are assumed to be ideal, which means that zero hinge stiffness is used. This assumption is satisfactory since almost all other simulations use the same assumption. The force-displacement and energy curves are compared for the three different thicknesses using the three different shell elements. In particular, the maximum values of the total strain energy curves Q of the different elements are compared and the percentage difference Dif between the hybrida element $Q(Z_{Hy})$ and the Abaqus $STRI3$ element $Q(Z_{Ab})$, which are close to each other in terms of the formulation, is presented and calculated by

$$Dif = \frac{Q(Z_{Ab}) - Q(Z_{Hy})}{Q(Z_{Hy})}.$$

The force-displacement and energy graphs for the three different thicknesses with the three shell elements are plotted in Figures 2.5, 2.6, and 2.7. The maximum values of the total strain energy curves are compared in Table 2.1 for different thicknesses and the difference Dif is calculated. It is shown that hybrida differs at maximum 2.4% from the $STRI3$ Abaqus element.

Table 2.1: Max values of total strain energy [Nm]
from shell element. The difference is defined as the percentage difference between the Hybrida and the Abaqus $STRI3$ element.

Thickness	10 %	5 %	2 %
hybrida	3.82	1.23	0.364
$S3$ Abaqus	3.63	1.24	0.354
$STRI3$ Abaqus	3.88	1.26	0.365
Difference	1.6%	2.4%	0.27%

In general, the results between hybrida and Abaqus compare well. Figure 2.5 shows that both Kirchhoff-Love elements do compare well and that the Mindlin-Reissner element shows a softer response. The difference between hybrida and the Abaqus $STRI3$ element for the 10% thickness is 1.6%. Figure 2.6 shows the force-displacement and energy graphs for 5% thickness and a difference is observed of 2.4%. Figure 2.7 shows the comparison for 2% thickness, the thinnest of the three tests. Here we see that the hybrida element and the Abaqus element differ only by 0.27%.

2.4. Manufacturing and testing of the Star bellow

Several prototypes are fabricated to demonstrate the bistability of the Star bellow structure and to perform load tests. The manufacturing and testing procedures for the Single and Double Star bellows are

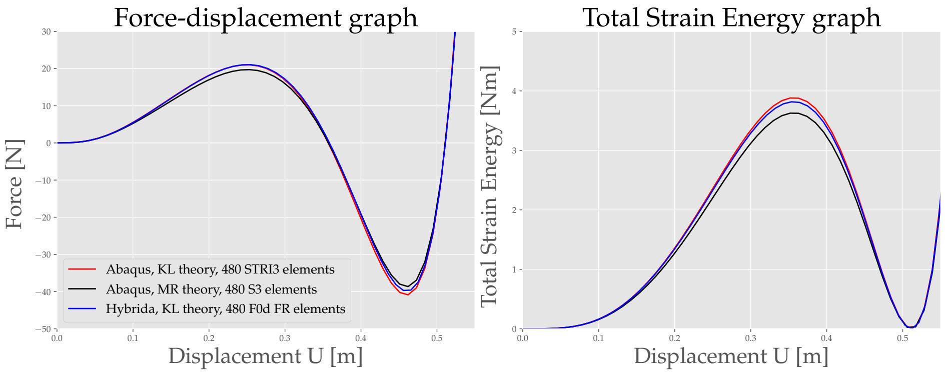

Figure 2.5: Comparing results of Hybrida and Abaqus for 10% thickness

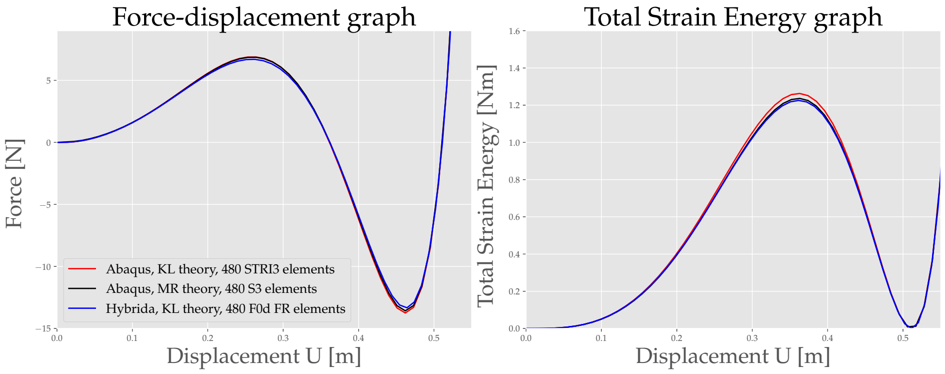

Figure 2.6: Comparing results of Hybrida and Abaqus for 5% thickness

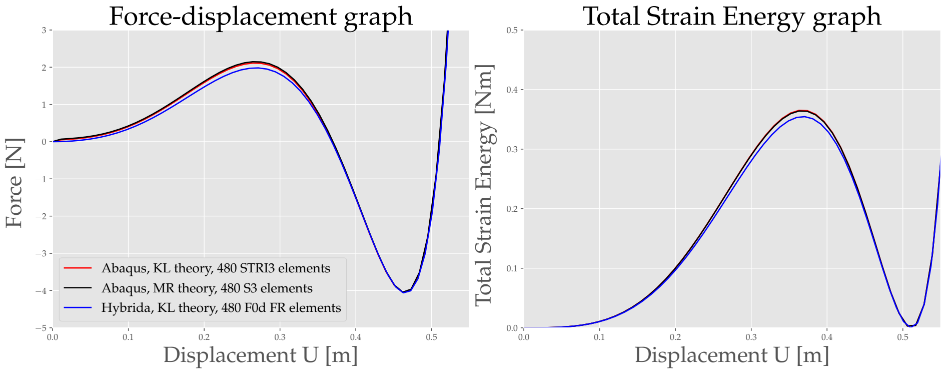

Figure 2.7: Comparing results of Hybrida and Abaqus for 2% thickness

similar. The prototypes of the Star bellow are made from different sheet (cardboard in the following example) materials with double-side sticky tape (23205-1009, Blick) in between. The double-side tape layer functions as hinge material. The shapes are laser cut with a CO2 laser system (VLS 2.3, Universal Laser Systems). A similar method was used by Overvelde [19, 62].

The first step in the manufacturing process is laser cutting the front and the back star shapes out of cardboard (step 1, figure 2.8) and removing them from the machine. The shapes are different which will create outskirts and openings. These are used in the assembly process to attach the star shaped layers together. The double-side tape is used in between the two parts of a star panel to stick the two paper parts together (step 2). Then the laser cutter is used to cut along the outer shape. This process is performed for two panels, since a Star bellow consists of two panels attached to each other. Now we end up with two identical star shaped panels which can be assembled (step 3). During the assembly, two small bolts are inserted at the center tips and the Star bellow is finished (step 4).

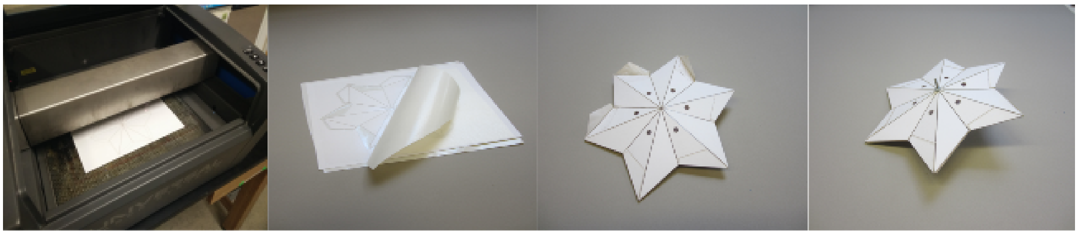

step 1) laser cutting step 2) double-sides tape step 3) assembly step 4) bolt and result

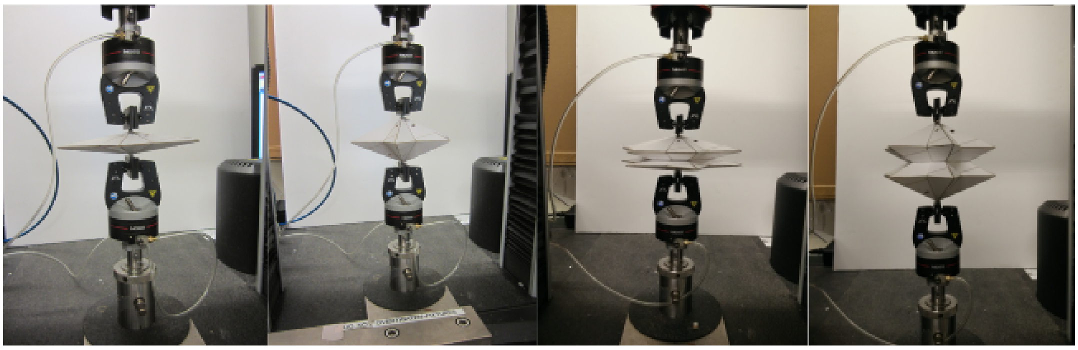

a) first stable point, single star b) second stable point, single star c) first stable point, double star d) second stable point, double star

Figure 2.8: Manufacturing and mechanical testing of star bellows

The mechanical testing is performed on an Instron universal testing machine (model 5566) with a $10\,N$ load cell. The Instron machine can measure loads with a maximum difference between a measured value and the true value of $0.0025\,N$. A cyclic loading method is used, which includes loading and unloading of the prototypes. The starting position of the test is chosen to be the first equilibrium position of the prototypes where the force is zero. The first equilibrium configuration of the prototypes is not always exactly the flat configuration, see figure 2.8.a and c. This is due to inaccuracies introduced in the manufacturing process. The prototypes are displaced to slightly above the second stable configuration to be sure the second stable position is reached, 2.8.b and d. Then the test continues with the unloading part. This cycle is performed three times in a row to be able to observe and confirm hysteresis behaviour. Both the Single and Double Star bellow are tested. The tests are performed in a vertical setup. This introduces an inaccuracy since gravity is weakening the bistability of the structure in this test setup.

Experiments are performed to estimate the Young's modulus of the material and the double-side tape combined, see figure 2.9.d. Four samples are used of 200 [mm] in length and 20 [mm] in width. The results are checked on consistency and the stresses and strains are calculated. The slope of the stress-strain curve is calculated for data in the linear regime. A linear regression function is used to calculate the slope of the stress-strain curve, which is the Young's modulus. The Young's modulus of the cardboard material including the double-side tape is estimated to be 982 [MPa].

An estimate for the hinge stiffness per unit length k [N/rad] is obtained via an experimental test. Figure 2.9.a defines the parameters. Characteristic hinge length w [mm] and width h [mm] are used. The force F [N] and the displacement u [mm] are measured by the testing machine. k is calculated by using the work balance and assuming that the faces do not bend or stretch [21]

$$\begin{aligned}
W_{in} &= W_{ex}\\
2\,k\,w\,\theta &= F\,u\\
\theta &= 2\ \arcsin\left(\frac{u}{h}\right)\\
k &= \frac{F\,u}{4\,w\ \arcsin\left(\frac{u}{h}\right)}.
\end{aligned}$$

The tests to estimate the hinge stiffness k resulted in a very low value. The results of the force showed such low values that the accuracy of the tests cannot be guaranteed in combination with the accuracy of the testing machine. Therefore, we assume the hinge stiffness k to be negligible.

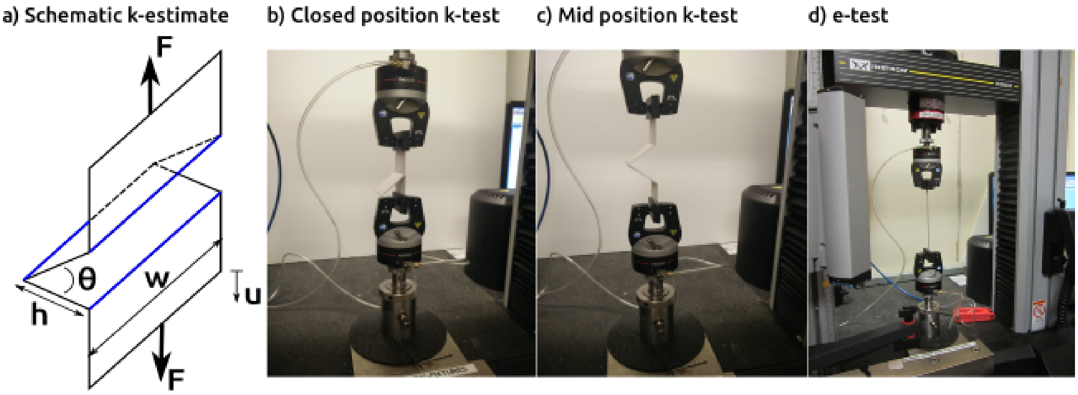
a) Schematic k-estimate b) Closed position k-test c) Mid position k-test d) e-test

Figure 2.9: k-estimate and e-estimate tests

2.5. Analysis and results of the Single Star bellow

Part of the research goal is to investigate the mechanical behaviour of the Single Star bellow by performing a parametric study, this is presented here. This is followed by physical load tests and FEM simulations. Based on these, a design improvement of the Single Star bellow is discussed.

2.5.1. Parametric study

The geometric and material parameters that will be studied for the Single Star bellow are shown in Table 2.2. Different shapes can be defined, which have alternating long and short, mountain and valley crease lines. Three different shapes are considered: the star, the quadrangle and the triangular shape, shown in Figure 2.10. The Cut-Backs of the shapes are scaled to be constant relative to the Star shape. The hinge width is also recognized as a geometric parameter, but it is chosen not to include this in the parametric study. It is kept constant because this parameter is set in combination with the material thickness.

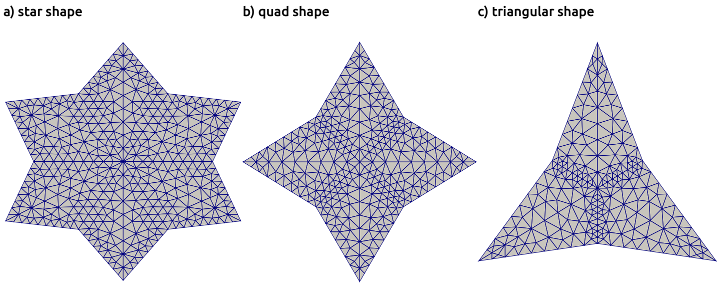
a) star shape b) quad shape c) triangular shape

Figure 2.10: Shapes

Table 2.2: Parameters overview for the Single Star bellow

Parameter	**Value range**
Shape	Tri, Quad, Star
Size	$0.8 \cdot l$, $1 \cdot l$, $1.2 \cdot l$ [mm]
Cut-Back (CB) size	0% - 40%
Hinge stiffness	0 - 100 [N/rad]
Young's modulus	600 - 3000 [MPa]
Panel thickness	0.5 % - 10 %

Monitoring quantities that are important for interpreting the results of the simulations are:

1. Von Mises stress distributions of the membrane and bending stresses to identify stress concentrations.
2. The value of the energetic minimum corresponding to the second stable configuration.
3. Minimum and maximum force values of the force-displacement graph.
4. The minimum value of the force is used as the main measure for the bistability since this parameter is directly measurable by the load tests and can be computed by the simulations. Furthermore, it is a direct measure of the bistability of a structure because it should be negative for the structure to be bistable. It is recognized that the slope of the force-displacement curve would also be a good measure for the bistability of the structure.

To gain understanding of the Star bellow's mechanical behaviour, the results of the parametric study using hybrida are presented. The Cut-Back has a major influence on the bistable properties of the Star bellow. The Cut-Back ranges from 0% to 40%. It is shown that a Cut-Back ranging from 20% to 30% is most interesting. If the Cut-Back is relatively small (under 20%) the deformations of the faces are so large that the material was shown to crumple in physical experiments. For relatively large Cut-Backs (above 30%), it is shown that the bistable behaviour gets very weak. The results of the Cut-Back variation are shown in Figure 2.11. It is noted that the Cut-Back has a large influence on the bistability: the smaller the Cut-Back, the larger the bistability. The hinge stiffness is another parameter of major influence. Several different hinge stiffness settings are simulated as shown in Figure 2.12. It is clear that the hinge stiffness influences the energy level of the second stable state since strain energy is stored in the hinges. For high hinge stiffnesses the bistability of the Star bellow is lost. Appendix A shows the remaining results of the parametric study.

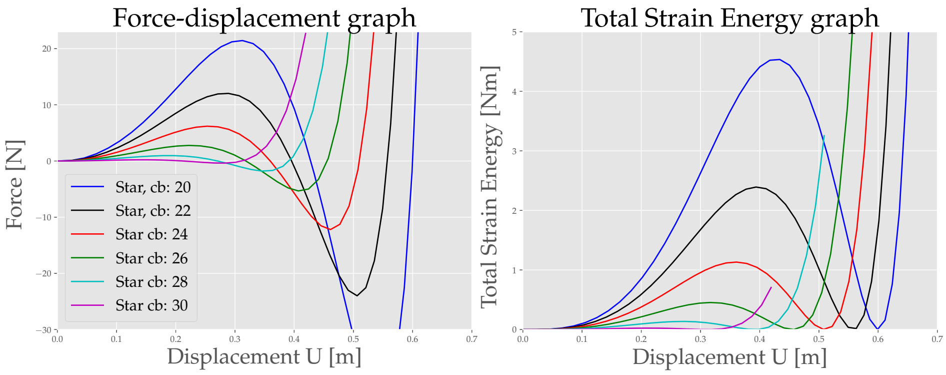

Figure 2.11: Cut-Back variation

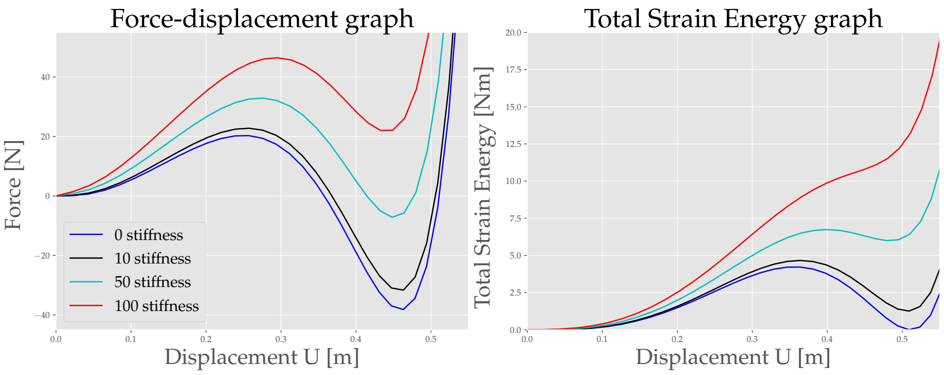

Figure 2.12: Hinge stiffness variation

2.5.2. Physical load testing of Single Star bellow prototype

The dimensions of the Single Star bellow prototype are chosen to be 88 [mm] for length l and a 24% Cut-Back. Experience from the past indicates that these values showed good results and easy handling. The thickness of the faces of the structure, including the double-side sticky tape is 0.8 [mm]. This corresponds with a 0.9% thickness to length l ratio. The Poisson’s ratio of the material is 0.3 and the Young’s modulus is 982 [MPa]. Figure 2.13 shows the resulting force-displacement curve of the load test of the initial and improved prototype in a combined plot. The improved prototype was a result of the design improvement, described in section 2.5.4. The black curve is the force-displacement curve of the initial design, the blue is the one of the improved design. The initial stable configuration of the prototypes was not flat, but had a ’pre’ displacement, measured from the symmetry plane. This is called the offset.

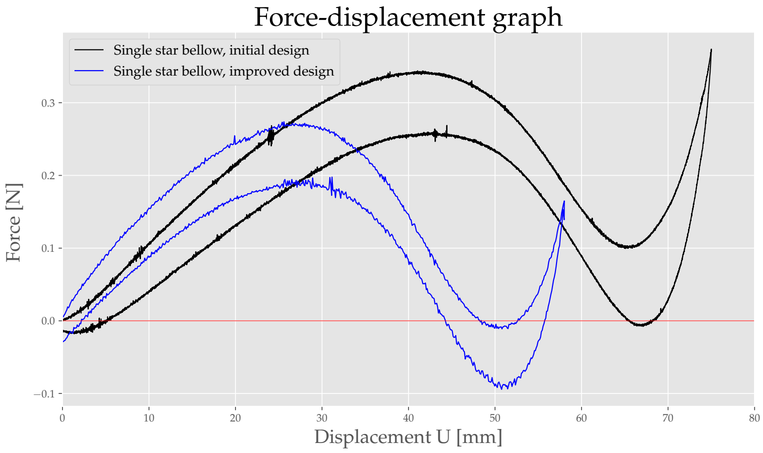

Figure 2.13: Resulting force-displacement graph of the physical load tests of the initial (Black) and improved (Blue) designs.

The loading and unloading path of the load tests are plotted for one cycle in Figure 2.13. The curve of the initial design shows snap-through behaviour, but the minimum force value never reaches zero. This indicates that the structure is not bistable, which is contradicting because the structure clearly shows bistability in observations. This strangle test result can be due to the vertical testing setup where gravity can weaken the bistability. The loading and unloading paths are different and show looping behaviour when multiple load cycles are performed, therefore mechanical hysteresis behaviour is confirmed (see section 1.4). Furthermore, the curves of the initial and improved design does not match with respect to the displacement. This is due to a manufacturing inaccuracy resulting in a larger offset of 18 [mm] for the improved design, compared with an offset of 15 [mm] for the initial design. Therefore, the displacement path is shorter for the improved design. The deformation path is therefore reduced and this could be the reason that the maximum force value is lower compared to the initial model.

Furthermore, Figure 2.13 shows that the minimum force value for the improved design is negative for the loading and unloading path, which is a requirement for bistability. The improvement in bistability of the improved design is indicated in terms of the decrease in the minimal force value. Compared to the initial design an improvement of 0.11 [N] is achieved.

2.5.3. FEM simulation of the Single Star bellow prototype

FEM simulations of the Single Star bellow initial and improved prototypes are performed. The goal is to check if the simulations matches the results from the load tests and to see if the simulations indicates that an improvement of the bistability is possible. A fine mesh of 20 elements per crease line is used to be able to examine the stress distributions of the membrane and bending stresses. The symmetry of the structure is used in the model. The membrane and bending Von Mises stresses are plotted separately. The resulting force-displacement curves are compared with the test results by checking the values and positions of the maxima and minima of the force. Furthermore, the membrane and bending strain energy is plotted separately to give insight in the distribution of the two energy types. Two models are used for the FEM simulations. One model has a closed tip as was used in the parametric study. The other model has a hole at the top with a diameter of 4 [mm] to match the test model more accurately.

The force-displacement and energy curve of the model of the initial prototype with top hole is shown in Figure 2.14. The strain energy graph shows the membrane and bending strain energies separately, indicating that the membrane deformation is dominant over the bending deformation. Furthermore, the membrane and bending Von Mises stress distributions are shown for both models in Figure 2.15. These plots show high membrane stresses at the tips and high bending stresses at the top of the structure. In addition, the physical load tests of the initial and improved prototype are compared with the results of the FEM simulation in Table 2.3. The results of the model without top hole are shown in the appendix in Figure B.1, together with a comparison between the two models in Table B.1. Comparing the FEM simulations of the Star bellow with and without top hole, show that the top hole, weakens the bistability.

Table 2.3: Results of the FEM simulation with top hole and the results of the physical load tests for the initial and the improved prototype are compared. The loading path of the test results is used for the comparison. The improvement in bistability is given in [N], calculated using the minimum force value of the initial and improved design load test results.

	Sim. initial	*Test initial*	*Sim. improved*	*Test imporved*	**Improvement**
Max. F [N]	7.12	0.34	9.30	0.27	-
U [mm]	35.93	40.25	20.57	25.00	-
Min. F [N]	-14.30	0.1	-16.22	-0.01	0.11
U [mm]	69.29	65.50	49.22	50.50	-

Comparing the numerical results with the load tests of Figures 2.14, 2.13, and by using Table 2.3, it was found that the numerical results do match the experimental results in terms of the displacement, but give an over-estimate of the force values. Furthermore, the shape of the curves compare well. Additionally, the FEM simulation of the Single Star bellow prototype is performed with hybrida and the Abaqus $S3$ shell element. The results compare well and the force-displacement and energy graphs are shown in the appendix, Figure B.2. This over-estimation of the force was also confirmed for the Abaqus $S3$ element. It is observed that during the manufacturing inaccuracies are introduced, this may weaken the bistability. Also, gravity could decrease the bistability during the load test, because of the vertical test setup. The gravity was not taken into account in the FEM simulations. Furthermore, the crease lines of the prototype have room to compress and stretch and therefore does not match the ideal hinge assumption used in the FEM implementation. These factors are identified to play a role in the difference between the numerical and experimental data.

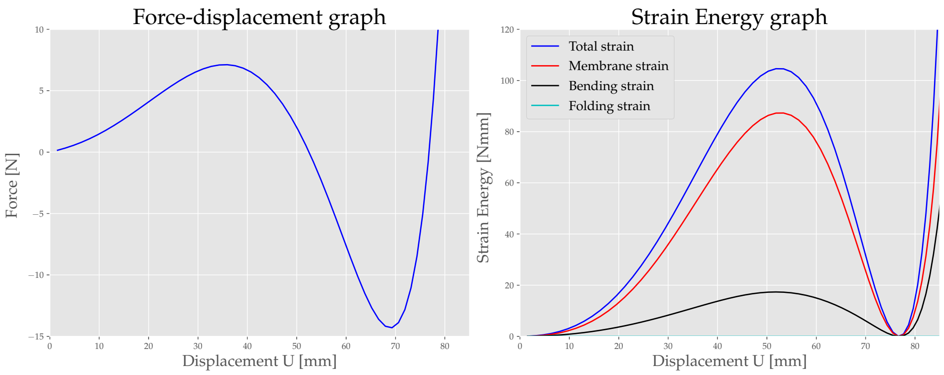

Figure 2.14: Initial design, Single Star bellow with top hole and offset of 15 [mm]

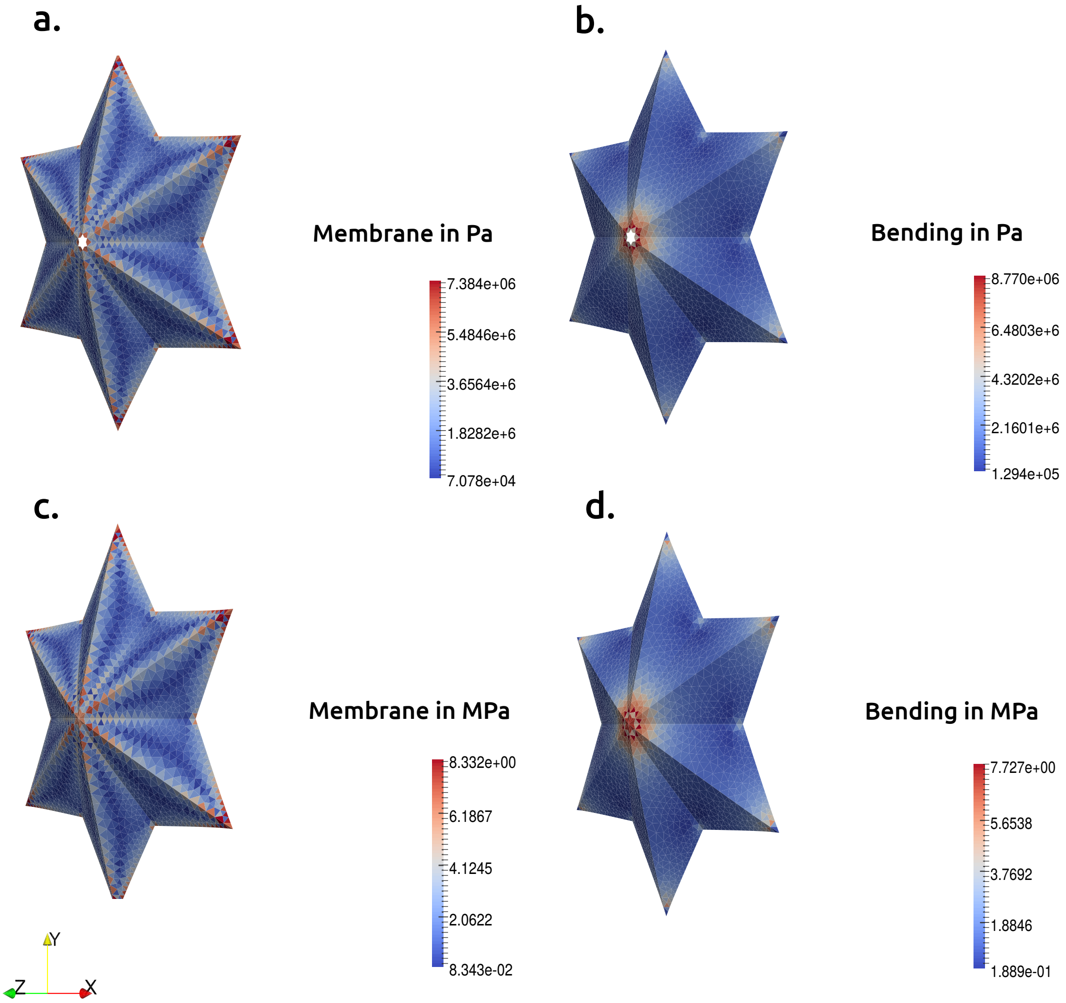
a.
Membrane in Pa
7.384e+06
5.4846e+6
3.6564e+6
1.8282e+6
7.078e+04
b.
Bending in Pa
8.770e+06
6.4803e+6
4.3202e+6
2.1601e+6
1.294e+05
c.
Membrane in MPa
8.332e+00
6.1867
4.1245
2.0622
8.343e-02
d.
Bending in MPa
7.727e+00
5.6538
3.7692
1.8846
1.889e-01
Y
Z
X

Figure 2.15: Figures a and b show respectively the Von Misses membrane and bending stresses in [Pa] for the model with top hole. Figures c and d show the Von Mises membrane and bending stresses in [MPa] for the model without top hole.

2.5.4. Design improvements and comparison

The results and observations from the load tests, the parametric study and the FEM simulations are evaluated and observations during the load tests showed slip of the connection between the top and bottom star panels at the star tips, see figure 2.16. This is supported by the Von Misses membrane stress distribution plots, which show high stress concentrations at the star tips, see Figure 2.15. This observation, the slip of the connection between the top and bottom star panels, is recognized to cause a weakening of bistability, because it reduces the deformation of the faces. By maximizing the deformation of the faces we aim to improve the bistable properties of the Star bellow.

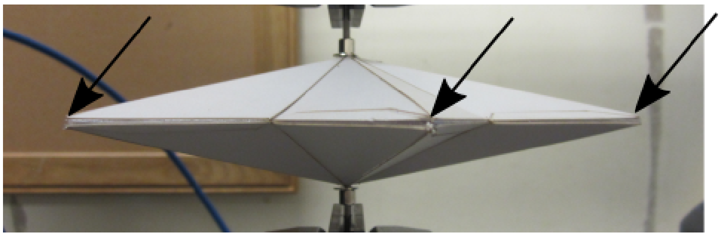

Figure 2.16: Testing initial Single Star bellow structure showing separation at tips

The design of the connection between the top and bottom star panels is changed. This design improvement is a structural change and not a change in the geometric parameters, although it is shown in the parametric study that a geometric change can improve the bistability as well. A structural change of the design is preferred because it can decrease the difference between the numerically predicted bistability and the resulting bistability from the physical tests. Furthermore, the results from earlier physical load tests are still comparable because the geometry of the initial and the improved Star bellows are similar.

2.6. Analysis and results of the Double Star bellow

The Single Star bellow is considered to be the unit cell. This unit cell is tessellated into a metamaterial. By FEM simulations and tests we aim to study the influence of the tessellation of the Star bellow on the bistable properties of the structure.

2.6.1. Extended parametric study for the Double Star bellow

The parametric study for the Double Star bellow is comparable to the one presented for the Single Star bellow. The parametric study is extended for one more parameter, the trim. The trim is defined as the percentage of the mountain crease line from were the top of the star bellow is removed, see Figure 1.3. The trim is varied for three values, 40%, 50% and 60%. The trimmed edges are constrained to stay planar, to mimic the conditions in a tessellation, which is accomplished by using Multiple Point Constrains. It is found that the bistability increases linearly with the decreasing trim percentage. Figure A.5, in the appendix, shows the results of the simulations with varying trim percentage.

2.6.2. Physical load testing of Double Star bellow

The improved design, developed in section 2.5.4, is used to manufacture the Double Star bellow. The load tests aimed to determine the influence of tessellating the Star bellow unit cell into a 1D-array. The Double Star bellow prototype has an offset of 30 [mm]. Figure 2.17 shows the force-displacement curve of the load tests of the Double Star bellow prototype. It is observed that the minimum force value is substantially higher compared with the Single Star bellow. The weaker bistable behaviour of the Double Star bellow is also illustrated by the lower negative slope of the force-displacement curve after the first limit point in the load. Observing the loading path of the test results of the Double Star bellow, similar to the initial Single Star bellow test results, the minimal force value does not reach zero. This is most likely due to the gravity which weakens the bistability. Additionally, the gravity effect for the Double Star bellow might influence the test results more than for the Single Star bellow.

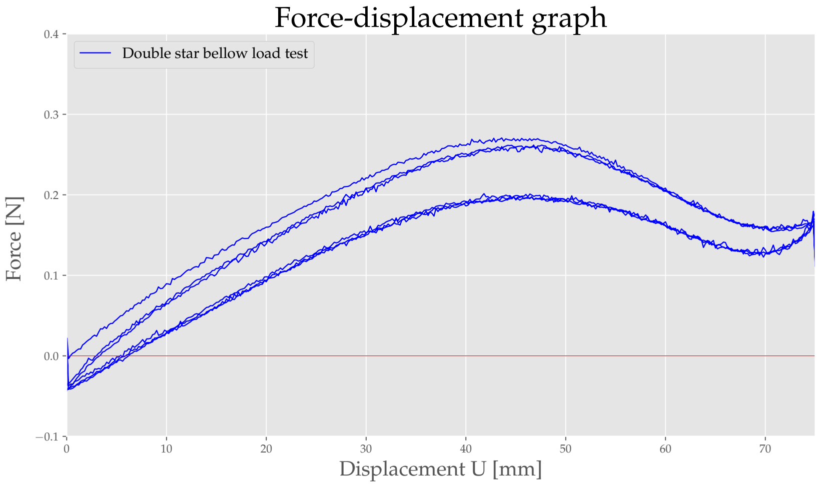

Figure 2.17: Resulting force-displacement graph of the load tests of the Double Star bellow prototype.

2.6.3. FEM simulations of Double Star bellow

FEM simulations are performed on the Double Star bellow, using two models. The first model consists of the Star bellow which is trimmed on both sides. This corresponds to a Star bellow unit cell in a tessellated 1D-array, as was illustrated in Figure 1.3.c. Periodic boundary conditions are applied on the trimmed edges by using Multiple Point Constrains (MPC). Figure 2.18 illustrate the position of the applied force on the master node and the application of the MPC to the periodic boundaries. This simulation investigates if the bistable property of the Star bellow unit cell is maintained when it is tessellated into a 1D-array. Furthermore, this simulation can show the influence of the tessellation on the symmetry of the structure, since no boundary conditions are applied on the outer geometric edges. For a description of the periodic boundary conditions in combination with the finite rotations shell elements, see appendix G. The second model is a full representation of the Double Star bellow, see Figure 2.19. The symmetry of the structure is used. This simulation investigates if the behaviour, shown by the physical load tests of the Double Star bellow, is represented in the results of the FEM simulation.

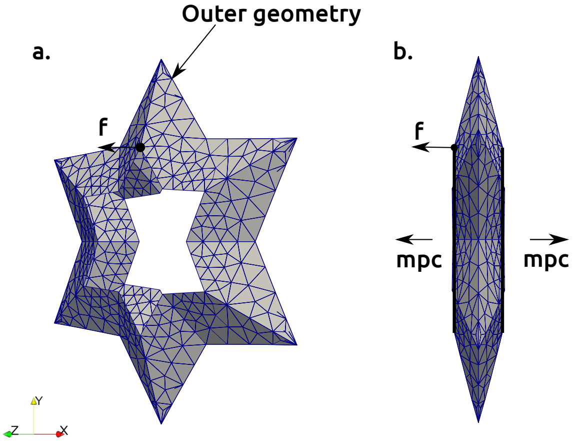

Figure 2.18: In the periodic model the load is applied on the master node and the displacement of this master nodes is applied on the symmetry edges by using Multiple Point Constrains.

The FEM simulation results of the periodic boundaries simulation are shown in Figure 2.20. The simulation indicate that bistable behaviour of the Star bellow unit cell structure is present. Furthermore, it is confirmed that the hinges in the unconstrained symmetry plane remain planar. The results of the

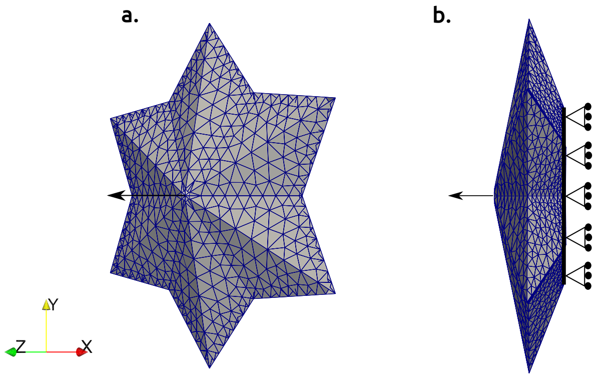

Figure 2.19: Mesh, load case and boundary conditions of the symmetric Double Star bellow model in deformed configuration.

symmetric Double Star bellow simulation are shown in Figure 2.21. The behaviour of the Double Star bellow load tests (Figure 2.17) and the FEM simulation are comparable, although a large over-estimate of stiffness of the structure is observed. The shapes of the force-displacement curves of the simulation and the load tests compare well. The two simulation models observe similar shapes and a small difference in the force and energy predictions. It is noted that the periodic boundaries model shows a steeper slope of the force-displacement graph than the symmetric model, indicating a stronger snap-through.

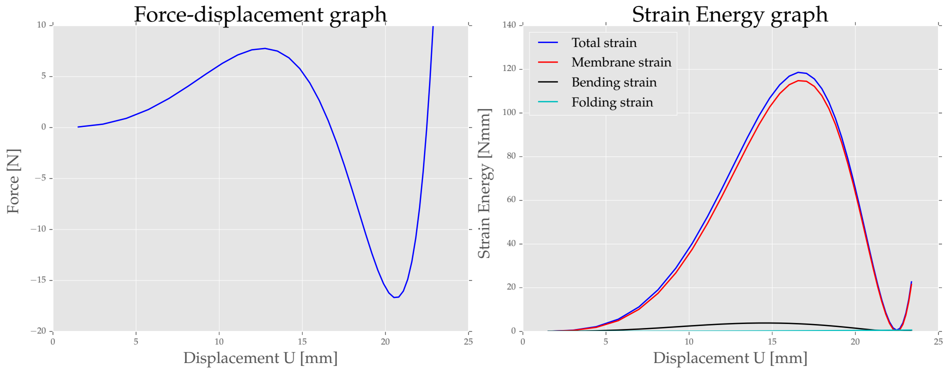

Figure 2.20: Simulation results of unit-cell Star bellow with periodic boundary conditions.

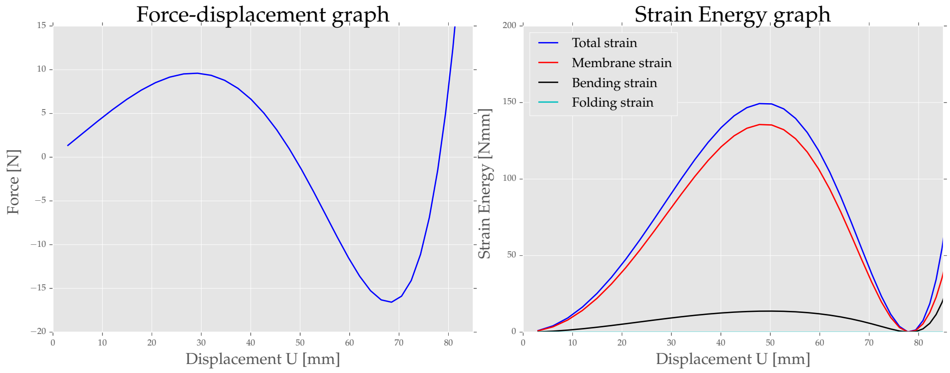

Figure 2.21: Simulation results of the symmetric Double Star bellow simulation.

The comparison in Table 2.4 shows that the displacement path of the Double Star bellow is longer, which was also expected. The minimum force value of the Double Star bellow is 0.159 [N] higher compared with the improved design Single Star bellow. This shows that the bistability is significantly reduced, but the bistable property is still observed in the load tests and FEM simulations. Because of the external influences as gravity and the manufacturing inaccuracies it is difficult to quantify how much the bistability is reduced.

Table 2.4: Comparison of the force values [N] of the loading path of the Double and Single Star bellow (improved design). The symmetric model is used to generate the Sim. double data.

	Sim. double	*Double*	*Sim. Single*	*Single*	**Difference**
Max. F [N]	9.95	0.27	9.30	0.27	-
U [mm]	29.33	44.80	20.57	25.00	-
Min. F [N]	−16.40	0.16	−16.22	−0.01	0.159
U [mm]	68.60	71.00	49.22	50.50	-

2.7. Conclusions

Understanding of the mechanical behaviour of the Star bellow structure was gained by performing a parametric study. The alternating long and short crease lines in combination with the structure's symmetry is shown essential to the bistable behaviour of the Star bellow structure. The Cut-Back is found to be the most important geometric parameter for influencing the bistable behaviour. The simulation functionality could plot membrane and bending strains separately and showed that the deformation of the Star bellow is dominated by membrane deformation.

FEM simulation indicated that there was room for improvement of the bistable properties of the Single Star bellow initial prototype. Based on the parametric study, FEM simulations, and load tests of the initial prototype, a design change was proposed to improve the bistability of the Single Star bellow. Although a geometric change could improve the bistability easily, a structural change to the Star bellow's design is made. Therefore, the load tests of the initial and new designs are still comparable. The minimum force value, which was identified as a measure of the bistability, was improved by 0.11 [N]. The bistability can still be improved more, which can be accomplished by performing more design improvement iterations.

The results of the FEM simulations are compared with the results of the load tests of the Star bellow prototypes. The FEM simulations over-estimate the force. This might be the result of inaccuracies in the manufacturing process of the prototype, the vertical load testing method, and the errors introduced by simplifying the behaviour of the crease lines. Although the force values between the simulations and the load tests do not compare well, the bistable characteristics, shown by the test results, are well represented by the simulations.

Load tests and FEM simulations on the Double Star bellow were performed to investigate the feasibility of tessellating the Star bellow unit cell into a 1D-array to create a mechanical metamaterial. The load tests of the prototype of the Double Star bellow show that the tessellation of the Star bellow into a metamaterial keeps its bistable characteristics, although the bistability is reduced compared to the Single Star bellow.

The application of the FEM approach as developed and used in this study is expected to be generally applicable to other origami structures and to the other class, rigid origami. Although, that is not investigated in this research. It is recognized that this FEM approach is most suitable to be applied to non-rigid origami. For the Star bellow, specifically, membrane deformation is dominant. The choice for using a membrane, instead of an shell element can therefore be considerer to reduce computation time.

2.8. Outlook

The following directions for further research are recommended and possible improvements are identified for the FEM approach implemented in hybrida.

First of all, one of the factors identified to weaken the bistability of the Star bellow structure were inaccuracies initiated during the manufacturing process. Improving the manufacturing methods to eliminate inaccuracies in the prototypes can improve the bistability of the Star bellow and might decrease the difference between the simulations and load test results. Therefore, further research in manufacturing techniques for bistable non-rigid origami structures is advised. This might also lead to the practical application of these structures in devices like switches or energy absorbers.

Furthermore, the current tessellation mechanism introduces difficulties in the manufacturing and is not practical if the Star bellow is tessellated in 3D. The bistability may be improved by tessellating the Star bellow differently and this might increase the applicability of the structure. Searching for different shapes and different ways of tessellating the unit cell, using the same bistable mechanism, might increase the bistability and applicability further.

Additionally, looking at the FEM implementation to simulate non-rigid origami structures, a better representation of a non-ideal hinge element, a fold element, is advised to advance the simulation capability of hybrida. Such a fold element would be able to take compression and stretching of the crease lines into account. This is expected to increase the accuracy of the results.

The hysteresis and energy absorption capability of the Star bellow can have promising future applications. In this thesis, these properties are little researched. Future work can focus on investigated hysteresis in bistable origami.

3

Reflection

In this chapter a reflection on the thesis work is given. First of all, the process of the thesis work is discussed. Secondly, the time line is presented and compared with the original planning. The third section includes the challenges which were faced during the thesis work and describes how these were tackled. Finally, the contributions to the department's FEM code hybrida are included.

3.1. Process

The work on this thesis started with a literature review on the modeling techniques for origami structures. Soon it became clear that FEM was less used compared to the analytic geometric and energy methods. Furthermore, it was recognized that FEM is especially suitable for modeling non-rigid origami where deformation of the faces of the structure plays a significant role in the behaviour of the structure. Influenced by my supervisors, the logical choice was to implement a shell element in the department's FEM code hybrida and use this in modeling and designing an origami structure. This became the research goal of my thesis.

The part of this thesis dedicated to the implementation work involved the implementation of a plate bending element and several versions of a shell element in hybrida. Ultimately, I implemented a finite rotation shell element with a consistent tangent operator. In addition, a Hinge connection element was implemented, based on a torsional spring element. This was necessary to model crease lines in origami structures. The implementations were tested and verified by exact solutions and benchmark problems. In this process I gained understanding of non-linear mechanics and in particular the formulation of plate and shell elements. Furthermore, I gained understanding and experience in programming in Python.

While implementing the shell elements in hybrida, I was searching for an origami structure to apply the new simulation functionality. The Bertoldi Group of the Harvard University, John A. Paulson School of Engineering and Applied Sciences is on the forefront of research in the field of engineering origami. From January 2017 untill April 2017 I visited the Bertoldi Group in Boston. I was involved in a project on a bistable non-rigid origami structure called the Star bellow. This structure exhibits two stable states and shows snap-trough behavior. The bistable and non-rigid behaviour of the Star bellow made this project an excellent test case for the FEM approach because the shell elements are particularity suitable to model thin, non-linear structures. I performed structural analysis using the new shell elements in the hybrida code to gain understanding of the structure's behaviour and to improve the design of the structure to obtain better bistable characteristics.

In addition to the numerical work, I spend much time making prototypes of the Star bellow and performed physical load tests to obtain experimental force-displacement curves. This was a great addition to the work, which was purely numerical until then. The experimental results showed that the results from the FEM simulations promised strong bistable behaviour, but in reality the bistability was marginal. When I arrived back in The Netherlands in April 2017, I finished the simulation work and started writing the thesis. I choose to use the new thesis format of the PME department for my thesis.

3.2. Time line

This thesis project stated in April 2016 with the literature review. During the autumn of 2016, I spend implementing the plate and shell elements in hybrida. This was finished just before I left to the USA for the internship at Harvard in January 2017. The internship took three months. The last three months of the thesis, April to June, I spend on writing the thesis. During the thesis work I had to finish two courses. This took about a month. Furthermore, I have been on vacation for three weeks on the Trans Siberian Express to Beijing. That was in September 2016.

Initially, I planned to finish at in the beginning of 2017. At the end I finished in July 2017. These extra months, I spent on the internship at Harvard.

Concluding, about 70% of this thesis work was spent on the implementation of the finite rotation shell element in hybrida. The remaining 30% was spent on the application of the shell elements and experimental work to the study of bistable non-rigid origami structures at Harvard University. My thesis took longer than expected due the extra internship at Harvard.

3.3. Challenges

During the implementation of the shell elements in the hybrida python FEM code, I faced several challenges. Learning coding in Python was one of them. Furthermore, I shifted operating systems to Linux Ubuntu. This introduced additional difficulties, but once I got used to use Ubuntu I could see the benefits over using Windows. The biggest challenge was to transform the theory on plate and shell elements to a practical, general, and efficient code. To implement shell elements correctly, you should have a very good understanding of the theory. Usually, taking a very simple example, and using that to understand the theory works best. The first version of the implementation in the code should be done while testing with this simple example. That helps speed up the implementation process and avoids errors.

A systematic way of working is essential to avoid errors in the code during the implementation work. Nevertheless, bugs are always possible. These bugs can be minimized by testing the code during the implementation frequently, after a couple of lines of code or a block of code.

Using simple examples, preferably with an exact solution, is essential to implement an element in a FEM code in an efficient manner. The selection of a simple example is surprisingly difficult. The example should be simple, but it should be able to show the characteristics you would like to test. The formulation of simple examples is challenging, in the beginning I jumped too quickly into difficult examples. The problem with difficult examples is that it is not possible to identify the error anymore. Professor van Keulen helped me formulate simple test examples to eliminate errors step by step. This was a major learning point for me and helped me in the rest of the coding and analysis work.

Error analysis is a difficult job during implementation work of a FEM code. The observation of a convergence rate which is just not high enough can be due to many things. A simple mesh is the first step in creating transparency. I always used a two element mesh with unity side lengths. Furthermore, a step by step procedure in checking the intermediate results of a simple example will make it possible to find errors efficiently.

Readability and maintainability is important if other people will work with your code in the future, but even for yourself it is important. Confusion is avoided by commenting the code.

Finally, an important issue in programming and especially within hybrida, where many people contribute to the code, is the integration of your code into the existing structure. In the beginning, when learning how hybrida works, it is difficult and confusing to navigate through the files and

Table 3.1: Plate and shell elements available in Hybrida

Element	**Description**
$KL0$	Plate element with an out-of-plane translation per node and a rotation per side
$F0d$	Plate element in 3D
$F0d - UL$	Shell element with an Updated-Lagrange formulation to determine changes of curvature.
$F0d - FR$	Shell element with a Finite Rotation formulation to determine changes of curvature.
$F0d - FR - C$	Shell element with a Finite Rotation formulation and a consistent tangent operator.

follow the flow of the code. Using print commands and systematically reading existing code helps to find the flow. Before an implementation it is helpful to make a 'design' of the flow and how it should integrate into the existing structure.

The experimental work, conducted at Harvard University, introduced additional challenges. I learned to operate the laser cutter and load testing machine. The fabrication work of the Star bellow prototype should be performed as accurately as possible to minimize the inaccuracies of the resulting prototype. This was a major challenge because these inaccuracies influenced the experimental results. To improve the accuracy of the manufacturing process I made a frame of thin wood so the star shapes, out of the laser cutter, could be positioned correctly.

3.4. Contributions

Several plate and shell elements have been implemented and tested in hybrida as part of this thesis and are available for use. Table 3.1 shows the elements and a description. All the elements are triangular.

I have implemented a Hinge element, based on a torsional spring to connect two shell elements. This makes it possible to simulate crease lines in origami structures in hybrida.

Finally, I have validated the hybrida code against the commercial code Abaqus, by using the Star bellow origami structure as test case. The results were satisfactory and showed good correspondence of the results and was comparable in computation time.

A

Additional parametric study results

Figure A.1 shown the force-displacement and energy graph for three different **shapes**, the star, the quad and the triangular shape. The star shape gives the best bistable behaviour. It is recognized that the quad and triangular shape could have better bistable properties if the Cut-Back is scaled differently.

Three different **sizes** are simulated. One relatively small and one relatively large compared to the symmetric single Star bellow model. Figure A.2 shows the results of the size variation. A linear relation is observed between the size and the maximum energy value.

A varying **Young's modulus** is simulated and the results are shown in Figure A.3.

Different **thickness** ratio's are simulated, see Figure A.4. For very thin material the bistability is very weak, because the structure cannot carry bending loads any more and therefore loses bistability.

The **trim** percentage is varied shown in Figure A.5. A linear relation between the trim parameter and the bistable behaviour is found.

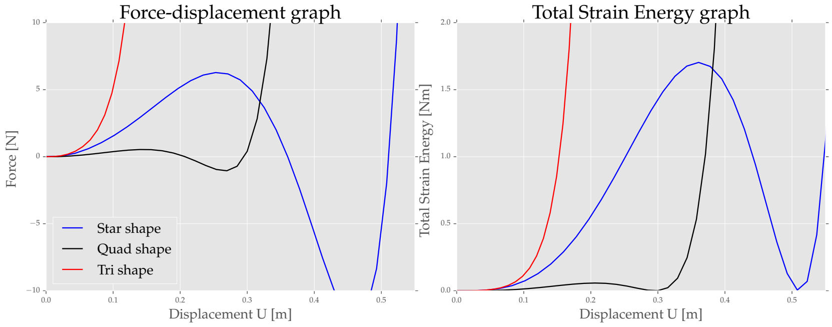

Figure A.1: Simulations with varying shape

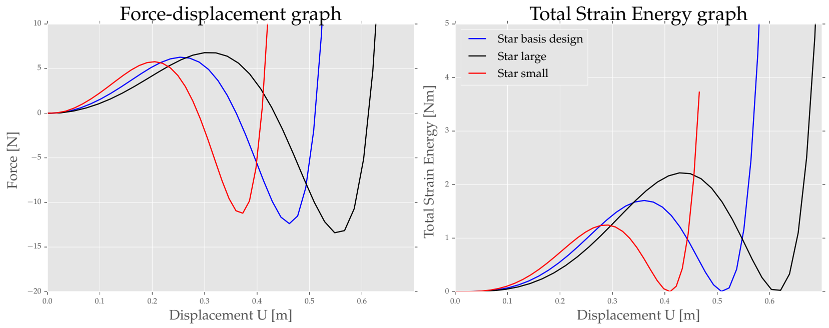

Figure A.2: Results of size variations

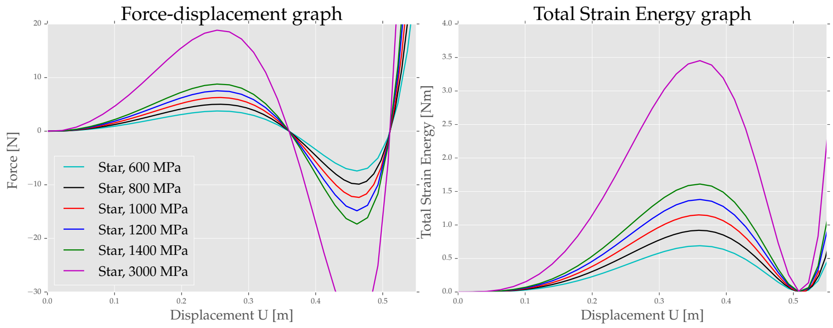

Figure A.3: Young's modulus variation

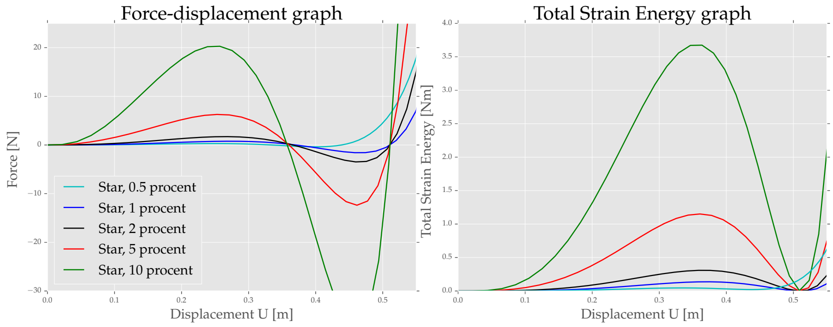

Figure A.4: Thickness variation

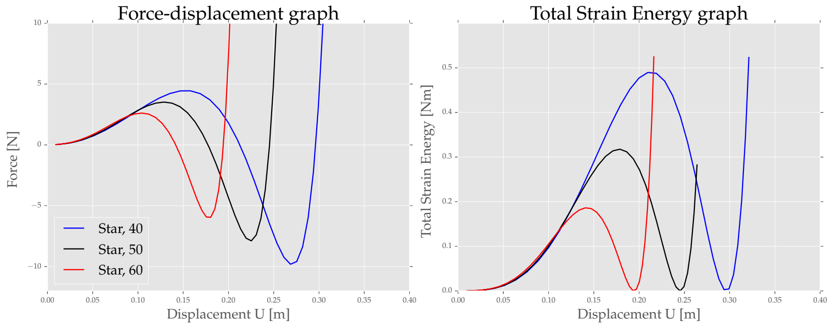

Figure A.5: Variation in trim

B

Additional FEM simulations

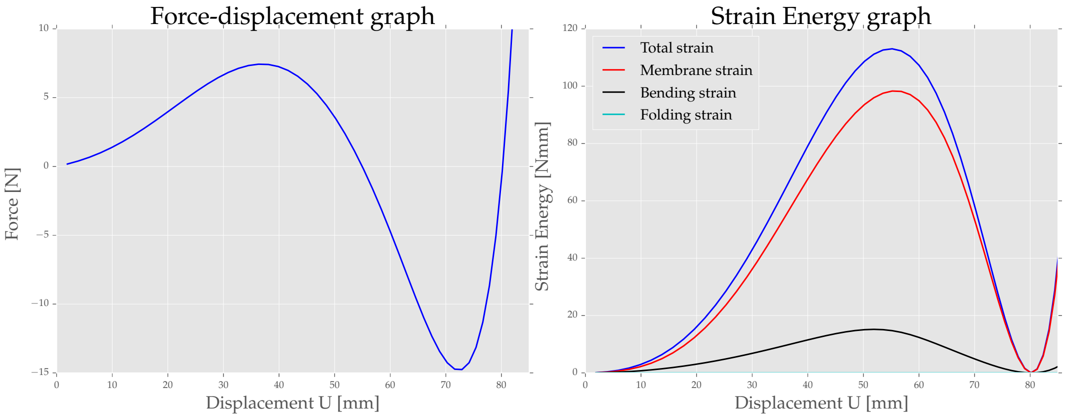

Figure B.1: Single Star bellow without hole

Table B.1: Results of the two simulation models, with and without top hole.

	Without hole	*With hole*
Max. F [N]	7.43	7.12
U [mm]	36.31	35.93
Min. F [N]	−14.76	−14.30
U [mm]	72.90	69.29
Max. E [Nmm]	113.03	104.60
U [mm]	55.18	51.83

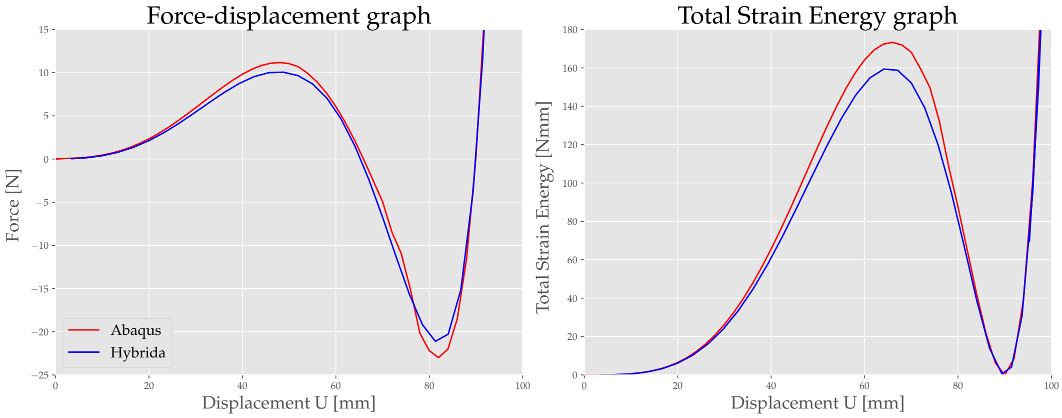

Figure B.2: Results of a FEM simulation of the star bellow prototype, with zero off-set, using the Hybrida and Abaqus *S3* shell elements.

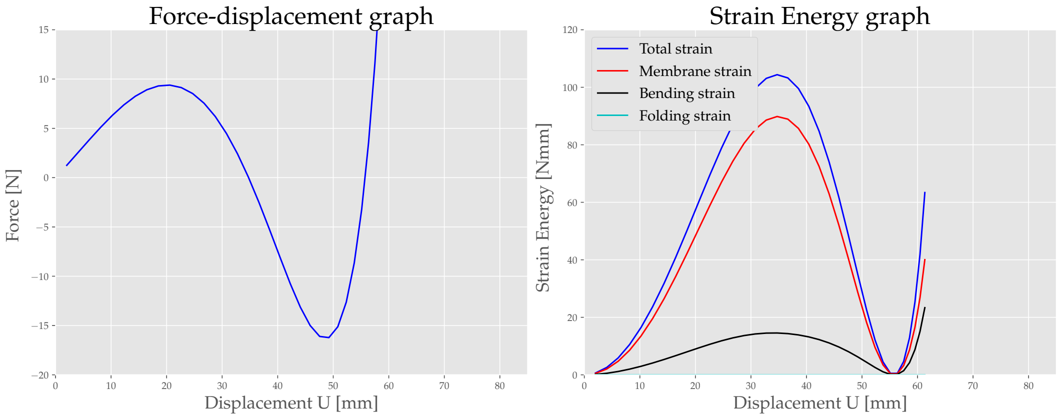

Figure B.3: Force-displacement graph of the FEM simulation of the improved design with an offset of 18 [mm].

C

An assumed stress hybrid beam finite element formulation

This appendix explains the assumed stress hybrid formulation for a beam finite element based on Euler-Bernoulli Beam theory (EBB). A beam element based on EBB theory can be formulated using a displacement approach in a convenient way, but the formulation of plate and shell elements based on the, comparable Kirchoff theory is troublesome [53, 63]. For the formulation of plate and shell element I adopt the assumed stress hybrid formulation in later appendices. To demonstrate the assumed stress hybrid formulation I would like to formulate an assumed stress hybrid beam element in this appendix and we will see that the resulting beam stiffness matrix is similar to the one derived by a common displacement approach.

Continuity requirements

The formulation of finite elements is subjected to continuity requirements. In EBB theory the second derivative of the displacement field $\frac{d^2w}{dx^2}$ is present in the internal energy functional which leads to the requirement of using C^1 continuous shape functions, see equation C.1. This requirement ensures that the displacement field $w(x)$ and the rotation field $\varphi(x)$ are continuous within the element en over inter-element boundaries. For displacement assumed beam elements this requirement is fulfilled by using hermitian shape functions [64]. An element which satisfies the continuity requirements is called conforming.

$$\Pi_p = \frac{1}{2}\int_0^L EI\left(\frac{d^2w}{dx^2}\right)^2 dx \tag{C.1}$$

Motivation for Hybrid elements

The formulation of conforming shape functions for plate and shell elements is troublesome [65], because the number of components of the shape function does not match the number of DOFs. This motivated engineers to develop the so called hybrid element formulations. The assumed stress formulation was first introduced by Pian [66] in 1964 and from there many scientists contributed to the development of hybrid methods. In the assumed stress hybrid element, continuity requirements are satisfied by introducing the continuity relations into the energy or virtual work formulation using Lagrange Multipliers instead of formulating conforming shape functions [53, 63]. In the following paragraphs we will show the derivation of a beam finite element using the assumed stress hybrid formulation.

Strong form

In this section the Strong Form (SF) equations for the beam using Euler-Bernoulli Beam theory will be summarized [67]. Consider a beam finite element as shown in Figure C.1.

The following unknown continuous fields are considered: displacement in the z direction $w(x)$, the rotation $\varphi(x)$, the curvature $\kappa(x)$, the moment $M(x)$ and the shear force $Q(x)$.

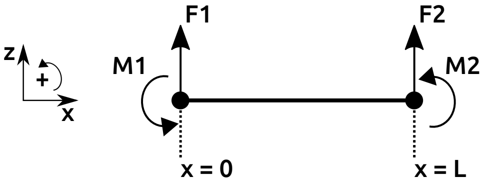

Figure C.1: Beam element

The assumptions used in EBB theory are:
1) The thickness t is relatively small compared to the length l.
2) The cross-section of the beam is constant.
3) The material is homogeneous, elastic and isotropic, therefore we apply Hook's law.
4) The deformation is small, so $(\frac{w}{t})^2 << \frac{w}{t}$.
5) Straight lines which are initially normal to the neutral-axis remain straight and normal after deformation, this leads to $\sigma_z = 0$ and $\tau_{xz} = 0$ and the kinematic equations C.2.

The kinematic equations are

$$\begin{aligned} \varphi(x) &= \frac{dw}{dx} \\ \kappa(x) &= \frac{d\varphi}{dx}. \end{aligned} \tag{C.2}$$

The constitutive equation is derived assuming a linear distribution of stress along the thickness of the beam, resulting in equation C.3. I is the area moment of inertia and E the Young's modulus. The moments act as a stress parameter and the curvature as a strain parameter.

$$\begin{aligned} M(x) &= \int_{-\frac{t}{2}}^{\frac{t}{2}} z\sigma dz \\ M(x) &= EI\kappa(x) \end{aligned} \tag{C.3}$$

The equilibrium equations are derived by taking a small slice of the cross-section of the beam and considering the moment field $M(x)$ and shear force field $Q(x)$ using a first order Taylor expansion. Then we use the general requirement for equilibrium, the sum of the forces and moments should be zero, see equation C.4.

$$\begin{aligned} &\sum M_y = -M + M + \frac{dM}{dx}dx - Qdx = 0 \quad && \frac{dM}{dx} = Q \\ &\sum F_z = -Q + Q + \frac{dQ}{dx}dx = 0 && \frac{dQ}{dx} = 0 \\ &\frac{d^2M}{dx^2} = 0 \end{aligned} \tag{C.4}$$

Boundary conditions are chosen in an appropriate way to derive the beam finite element, see figure C.1 and equations C.5.

$$\begin{aligned} M(x=0) &= M_1 \\ M(x=L) &= M_2 \\ Q(x=0) &= F_1 \\ Q(x=L) &= F_2 \end{aligned} \tag{C.5}$$

Assumed stress hybrid beam element

The potential energy formulation for a beam is defined in equation C.6. With the curvature κ, the bending moments M and the contribution of the external forces W. The derivation of the equation is a result of weakening a selection of the SF equations and is performed in the literature [67].

$$\begin{aligned} \Pi_p &= \frac{1}{2}\int_0^L EI\,\kappa^2\,dx - W \\ W &= F_1 w_1 + F_2 w_2 + M_1\varphi_1 + M_2\varphi_2 \end{aligned} \tag{C.6}$$

As mentioned above we add Lagrange multipliers λ_1 and λ_2 to introduce the continuity relations (C.2) into the formulation. This results in the modified potential energy formulation Π_{mp}. This ensures that the continuity relations are satisfied, but we are not obligatory to formulate conforming shape functions. A similar procedure is described in [68], see equation C.7.

$$\Pi_{mp} = \int_0^L \frac{1}{2} EI\,\kappa^2 + \lambda_1 \left(\frac{d\varphi}{dx} - \kappa \right) + \lambda_2 \left(\frac{dw}{dx} - \varphi \right) dx - W \tag{C.7}$$

An interpretation for the Lagrange multipliers is sought by taking the first variation of Π_{mp} with respect to κ and φ. As shown below, this results in an interpretation for λ_1 as the bending moments and for λ_2 as the transverse shear force. Note that for simplification we use the product rule and the definitions: a variation δ is never zero and a variation at the boundary is by definition zero.

$$\begin{aligned} \delta\Pi_{mp} &= \frac{\partial \Pi_{mp}}{\partial \kappa}\,\delta\kappa = 0 \\ &= \left(\int_0^L EI\,\kappa - \lambda_1\,dx \right) \delta\kappa = 0 \\ \lambda_1 &= EI\,\kappa \\ \lambda_1 &= M \end{aligned} \tag{C.8}$$

and

$$\begin{aligned} \delta\Pi_{mp} &= \frac{\partial \Pi_{mp}}{\partial \varphi}\,\delta\varphi = 0 \\ &= \left(\int_0^L \frac{dM}{dx} - \lambda_2\,dx\,[M]_0^L - M_1 - M_2 \right) \delta\kappa = 0 \\ \lambda_2 &= \frac{dM}{dx} \\ \lambda_2 &= Q \end{aligned} \tag{C.9}$$

We substitute (C.8) and (C.9) into (C.7). We also substitute the constitutive relation (C.3). This results in a functional equivalent to the modified complementary energy functional Π_{mc}.

$$\Pi_{mc} = \int_0^L -\frac{1}{2}\frac{M^2}{IE} + M\frac{d\varphi}{dx} + Q\left(\frac{dw}{dx} - \varphi\right) dx + W$$

Substitute $\frac{dM}{dx} = Q$

$$\Pi_{mc} = \int_0^L -\frac{1}{2}\frac{M^2}{IE} + M\frac{d\varphi}{dx} - \frac{dM}{dx}\frac{dw}{dx} + \frac{dM}{dx}\varphi\,dx + W$$

We use the product rule and bring a term outside of the integral $M\frac{d\varphi}{dx} + \frac{dM}{dx}\varphi = \frac{d}{dx}(M\varphi)$

$$\Pi_{mc} = \int_0^L -\frac{1}{2}\frac{M^2}{IE} - \frac{dM}{dx}\frac{dw}{dx}\,dx + [M\varphi]_{x=0}^{x=L} + W$$

We use the product rule again $-\frac{dM}{dx}\frac{dw}{dx} = \frac{d^2M}{dx^2}w - \frac{d}{dx}\left(\frac{dM}{dx}w\right)$

$$\Pi_{mc} = \int_0^L -\frac{1}{2}\frac{M^2}{IE} + \frac{d^2M}{dx^2}w\,dx + [M\varphi]_{x=0}^{x=L} - \left[\frac{dM}{dx}w\right]_{x=0}^{x=L} + W \tag{C.10}$$

In the given derivation we have introduced the continuity relation by means of Lagrange Multipliers and gone through several simplification steps to bring terms defined within the integral to the boundary terms of the formulation. These boundary terms are called the interface potential. From here we can start the discretization.

Discretization
We introduce a linear interpolation for the moment field $M(x)$

$$M(x) = \begin{bmatrix} 1-\eta & \eta \end{bmatrix} \mathbf{M}$$

$$\mathbf{M} = \begin{bmatrix} M_1 \\ M_2 \end{bmatrix} \qquad \eta = \frac{x}{L}$$

$$dx = L d\eta$$

$$\frac{dM}{dx} = \begin{bmatrix} -\frac{1}{L} & \frac{1}{L} \end{bmatrix} \begin{bmatrix} M_1 \\ M_2 \end{bmatrix}$$

We write the final modified complementary energy functional in matrix form

$$\Pi_{mc} = -\frac{1}{2}\mathbf{M}^T\mathbf{A}\mathbf{M} - \mathbf{M}^T\mathbf{B}\mathbf{u} - \mathbf{u}^T\mathbf{f} \tag{C.11}$$

with

$$-\frac{1}{2}\mathbf{M}^T\mathbf{A}\mathbf{M} = \int_0^L -\frac{1}{2}\frac{1}{EI}M^2 dx$$

$$-\mathbf{M}^T\mathbf{B}\mathbf{u} = +[M\varphi]_{x=0}^{x=L} - \left[\frac{dM}{dx}w\right]_{x=0}^{x=L}$$

$$-\mathbf{u}^T\mathbf{f} = -F_1 w_1 - F_2 w_2 - M_1\varphi_1 - M_2\varphi_2$$

Now we perform the interpolation for the three terms in Π_{mc}.

The first term

$$-\frac{1}{2}\mathbf{M}^T\mathbf{A}\mathbf{M} = \int_0^L -\frac{1}{2}\frac{1}{EI}M^2 dx$$

$$-\frac{1}{2}\frac{L}{EI}\int_0^1 \left(\begin{bmatrix} 1-\eta & \eta \end{bmatrix} \begin{bmatrix} M_1 \\ M_2 \end{bmatrix} \right)^2 d\eta$$

$$-\frac{1}{2}\frac{L}{EI}\frac{1}{3}\left(M_1^2 + M_1M_2 + M_2^2\right)$$

$$\mathbf{M}^T\mathbf{A}\mathbf{M} = \frac{1}{3}\frac{L}{EI}\left(M_1\left(M_1 + \frac{1}{2}M_2\right) + M_2\left(M_2 + \frac{1}{2}M_1\right)\right)$$

$$\begin{bmatrix} M_1 & M_2 \end{bmatrix} \frac{L}{EI} \begin{bmatrix} \frac{1}{3} & \frac{1}{6} \\ \frac{1}{6} & \frac{1}{3} \end{bmatrix} \begin{bmatrix} M_1 \\ M_2 \end{bmatrix}$$

Second term

$$
\begin{aligned}
-\mathbf{M}^T\mathbf{Bu} = {} & [M\varphi]_{x=0}^{x=L} - \left[\frac{dM}{dx}w\right]_{x=0}^{x=L} \\
& M_2\varphi_2 - M_1\varphi_1 + \frac{dM}{dx}w_2 - \frac{dM}{dx}w_1 \\
& M_2\varphi_2 - M_1\varphi_1 + \left(-\frac{1}{L}M_1 + \frac{1}{L}M_2\right)w_2 - \left(-\frac{1}{L}M_1 + \frac{1}{L}M_2\right)w_2 \\
& \begin{bmatrix} -\tfrac{1}{L}M_1 + \tfrac{1}{L}M_2 & -M_1 & +\tfrac{1}{L}M_1 - \tfrac{1}{L}M_2 & M_2 \end{bmatrix} \begin{bmatrix} w_1 \\ \varphi_1 \\ w_2 \\ \varphi_2 \end{bmatrix} \\
& \begin{bmatrix} M_1 & M_2 \end{bmatrix} \begin{bmatrix} -\tfrac{1}{L} & -1 & +\tfrac{1}{L} & 0 \\ +\tfrac{1}{L} & 0 & -\tfrac{1}{L} & 1 \end{bmatrix} \begin{bmatrix} w_1 \\ \varphi_1 \\ w_2 \\ \varphi_2 \end{bmatrix}
\end{aligned}
$$

Third term

$$
-\mathbf{u}^T\mathbf{f} = -F_1w_1 - F_2w_2 - M_1\varphi_1 - M_2\varphi_2
$$

$$
\mathbf{u}^T\mathbf{f} = \begin{bmatrix} w_1 & \varphi_1 & w_2 & \varphi_2 \end{bmatrix} \begin{bmatrix} F_1 \\ M_1 \\ F_2 \\ M_2 \end{bmatrix}
$$

We can take the first variation of the modified complementary energy functional in matrix form (C.11) to its dependent variables, **M** and **u**. We would like a relation between the moments **M** and the nodal displacements **u** and to do so we take the variation to **M**

$$
\begin{aligned}
\delta\Pi_{mc} &= \frac{\partial\Pi_{mc}}{\partial\mathbf{M}}\,\delta\mathbf{M} = 0 \\
&(\mathbf{MA} - \mathbf{Bu})\,\delta\mathbf{M} = 0 \\
&\mathbf{AM} = -\mathbf{Bu} \\
&\mathbf{M} = -\mathbf{A}^{-1}\mathbf{Bu}
\end{aligned}
\tag{C.12}
$$

We substitute the expression for **M** in terms of the nodal displacements **u** of equation (C.12) into the final complementary energy expression in matrix form (C.11) and compute the first variation to the nodal displacements **u** to derive the stiffness matrix

$$
\begin{aligned}
\Pi_{mc} &= -\frac{1}{2}\mathbf{M}^T\mathbf{AM} - \mathbf{M}^T\mathbf{Bu} - \mathbf{u}^T\mathbf{f} \\
&\quad -\frac{1}{2}\mathbf{u}^T\mathbf{B}^T\mathbf{A}^{-1}\mathbf{Bu} + \mathbf{u}^T\mathbf{B}^T\mathbf{A}^{-1}\mathbf{Bu} - \mathbf{u}^T\mathbf{f} \\
\delta\Pi_{mc} &= \frac{1}{2}\mathbf{u}^T\mathbf{B}^T\mathbf{A}^{-1}\mathbf{Bu} - \mathbf{u}^T\mathbf{f} = 0
\end{aligned}
$$

Leads to

$$
\begin{aligned}
&\mathbf{Ku} = \mathbf{f} \\
&\mathbf{K} = \mathbf{B}^T\mathbf{A}^{-1}\mathbf{B}
\end{aligned}
$$

with

$$\mathbf{B} = \begin{bmatrix} -\frac{1}{L} & -1 & +\frac{1}{L} & 0 \\ +\frac{1}{L} & 0 & -\frac{1}{L} & 1 \end{bmatrix}$$

$$\mathbf{A} = \frac{L}{EI}\begin{bmatrix} \frac{1}{3} & \frac{1}{6} \\ \frac{1}{6} & \frac{1}{3} \end{bmatrix}$$

The final stiffness matrix is given by matrix (C.13). It is similar to beam stiffness matrices derived with a common displacement approach] [64]. This demonstrated the principle of the assumed stress hybrid formulation for beam elements which will be adopted in the formulation of plate and shell elements in the following appendices.

$$\mathbf{K} = \begin{bmatrix} \frac{12EI}{L^3} & \frac{6EI}{L^2} & -\frac{12EI}{L^3} & \frac{6EI}{L^2} \\ \frac{6EI}{L^2} & \frac{4EI}{L} & -\frac{6EI}{L^2} & \frac{2EI}{L} \\ -\frac{12EI}{L^3} & -\frac{6EI}{L^2} & \frac{12EI}{L^3} & -\frac{6EI}{L^2} \\ \frac{6EI}{L^2} & \frac{2EI}{L} & -\frac{6EI}{L^2} & \frac{4EI}{L} \end{bmatrix} \tag{C.13}$$

D

A constant moment plate bending element

In this appendix we derive a constant moment plate bending element based on Kirchhoff-Love (KL) plate theory. The derivation is comparable to the assumed stress hybrid beam finite element of appendix C. We start by providing background information and definitions. Then we derive the finite element equations and discuss the implementation of a plate bending element, called $KL0$, in the python based finite element code framework hybrida. Finally, we present the results of numerical tests.

Plates versus shells
Plate- and shell elements are structural elements to model thin structures. Both use bending moments M and shear forces Q in structural calculations. The difference between plates and shells is that for plates the load carrying capacity is coming from the material properties only. Therefore, plates are restricted to small deformations and the linear regime. For shells the load carrying capacity comes from the material properties and from its geometry. This involves non-linearities. Another difference is that for plates we assume a flat initial configuration in the x, y plane and for shell its initial configuration can be curved and arbitrary positioned in space.

Categorization
Plate and shell problems are categorized by two parameters, relative thickness $\frac{h}{l}$ and relative deformation $\frac{w}{h}$. l is the characteristic length scale of the plate. h is the thickness and w is its out of plane deformation.

First we classify by relative thickness then by relative deformation. This results in the following classes:

1. If $\frac{h}{l} \geq 0.1$ we should think about **solid elements**
2. If $0.01 \leq \frac{h}{l} \leq 0.1$ we can use **plate and shell elements**
    (a) If $\frac{w}{h} \leq 0.25$ the deformations are small and we talk about **stiff plates**.
    (b) If $\frac{w}{h} \geq 0.25$ the deformations are large and we talk about **flexible plates**.
3. If $\frac{h}{l} \leq 0.01$ we talk about **membranes** which are very thin and can not carry load by bending moments

Within the plate and shell elements category we can differentiate between thick and thin plates or shells. We talk about thick plates or shells if $\frac{h}{l} \geq 0.07$. Otherwise we talk about thin plate or shell problems.

Historical note
As mentioned before, hybrid methods were introduced in the early sixties. The assumed stress hybrid formulation as we use it emerged a little later. Bazeley *et al.* published an article in 1966 describing

three plate bending elements using a displacement approach. Two of them were conforming elements. The conforming formulation was established by using numerical 'tricks' and were computationally inefficient. Surprisingly, the non-conforming element was reasonably accurate and efficient. The non-conforming element simply ignored the continuity requirement for the inter-element displacements. This motivated Morley to derive a non-conforming constant moment plate bending element based on quadratic interpolations for the displacements which was simpler than the formulations known at the time. He showed that the result using a displacement approach was the same as a formulation starting from complementary energy and adding the continuity requirements by Lagrange multipliers. This showed that the continuity requirements could be satisfied in an alternative way [63].

Plate bending models

A mathematical model is used to reduce the 3D structural element to a 2D mathematical model. To do this, assumptions are made to simplify the model. Two mathematical models are frequently used to describe plate bending.

The Kirchhoff-Love plate bending model is used for thin plates. The model assumes small deflections and a large wave length of the deformation of the plate. Therefore, shear strains are negligible.

The Mindlin-Reissner (MR) plate bending model is used for thick plates and plates were the wave length of the deformation is short. Therefore, transverse shear can play a significant role in the behaviour of the plate. The MR plate bending model takes transverse shear into account to improve accuracy of the model [69].

Kirchhoff-Love plate theory

When we compare plates with beams they are very similar. The Kirchhoff-Love plate theory is basically a 2D version of the Euler-Bernoulli beam theory discussed in appendix C. The important insight here is that we can not make a plate out off stagging beams next to each other. The beams stay 1D structural elements where as the plate has internal influences in 2D. In a plate the loads are distributes in two direction. The twisting moment M_{xy} takes care of this. Furthermore, the strains have a two dimensional effect on the stresses due to the constitutive relation.

We define the plate as an initially flat plate in the x, y plane of the global coordinate system. Therefore the out of plane or transverse deformation w is in the z direction. The plate is bounded by parallel planes. The 3D plate is reduced to a 2D mid-surface. Thickness h of the plate is constant and is small relative to the characteristic length l. Loads act perpendicular to the plate in the z direction.

We have a closer look at the assumptions of the general behaviour of plates. These assumptions are known as the Kirchhoff assumption and allow us to do 2D analysis of a 3D structure.

1. The material is homogeneous, elastic and isotropic, we apply Hook's law.
2. The deformation is small, so $(\frac{w}{h})^2 << \frac{w}{h}$.
3. Material which is initially normal to the mid-surface remain straight and normal after deformation of the mid-surface, see Figure D.1.
4. $\sigma_z = 0$, this is coming from the 'constant thickness' and 'straight normals' assumptions.
5. No axial strains of the mid-surface, because the displacements are small.
6. $\gamma_{xz} = \gamma_{yz} = 0$, no twisting of the sides, coming from the 'straight normals' assumption.

Coordinate systems

A global Cartesian coordinate system is used, defined by the base vectors $(\mathbf{e}_x, \mathbf{e}_y, \mathbf{e}_z)$. A local element coordinate system is used per element, defined by the base vectors $(\mathbf{e}_1, \mathbf{e}_2, \mathbf{n})$. With $\mathbf{n}$ the normal to the initial plates surface, $\mathbf{e}_1$ parallel to the element side 1 and $\mathbf{e}_2$ orthogonal to $\mathbf{e}_1$ and $\mathbf{n}$. A third coordinate system is defined at each element side given by the two vectors $(\mathbf{s}^i, \mathbf{t}^i)$. With $\mathbf{s}$ defined tangential to the element side and $\mathbf{t}$ normal to the element side. $i = 1, 2, 3$ denotes the three sides per element.

An in-plane second-order tensor is defined which represent the moment field $M_{\alpha\beta}$, with $\alpha, \beta = 1, 2$. The moment field can be represented with respect to the local element coordinate system $\mathbf{e}_\alpha$, with

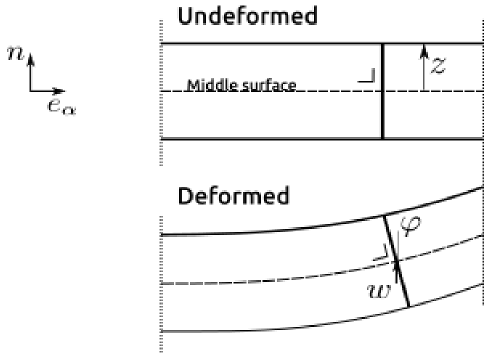

Figure D.1: Definition of KL theory, w and φ variables

$\alpha = 1,2$, as

$$M = \begin{bmatrix} M_{11} & M_{12} \\ M_{21} & M_{22} \end{bmatrix}$$

or with respect to the local element sides i of an element

$$M^i = \begin{bmatrix} M^i_{nn} & M^i_{ns} \\ M^i_{sn} & M^i_{ss} \end{bmatrix}.$$

A coordinate transformation is used to transform the tensor between the in-plane system and the system associated with the element sides. This transformation is shown in (D.1). Per element side i coefficients a_i and b_i are used. The coefficients a_i represent the projection of the sides on the element base vector $\mathbf{e}_1$. The coefficient b_i represents the projection of the element sides on base vector $\mathbf{e}_2$. λ denotes the length of the element side [53].

$$\begin{bmatrix} M^i_{nn} & M^i_{ns} \\ M^i_{sn} & M^i_{ss} \end{bmatrix} = \frac{1}{\lambda_i^2} \begin{bmatrix} -b_i & -a_i \\ a_i & -b_i \end{bmatrix} \begin{bmatrix} M_{11} & M_{12} \\ M_{21} & M_{22} \end{bmatrix} \begin{bmatrix} -b_i & a_i \\ -a_i & -b_i \end{bmatrix} \tag{D.1}$$

Strong form Kirchhoff-Love theory

The following derivation mainly follows the work by van Keulen [53]. The material in the mid-surface lay in the plane $z = 0$ and undergoes an out of plane displacement $w(x,y)$ along the z axis of the global coordinate system. The kinematic relations are defined as

$$\begin{aligned} \varphi_\alpha &= w_{,\alpha} \\ \kappa_{\alpha\beta} &= \frac{1}{2}\left(\varphi_{\alpha,\beta} + \varphi_{\beta,\alpha}\right) \end{aligned} \tag{D.2}$$

The constitutive relation for linear elastic isotropic homogeneous material behaviour reads

$$\begin{aligned} \begin{bmatrix} M_{11} \\ M_{22} \\ M_{12} \end{bmatrix} &= E_b \begin{bmatrix} \kappa_{11} \\ \kappa_{22} \\ 2\kappa_{12} \end{bmatrix} \\ E_b &= \frac{Eh^3}{12(1-v^2)} \begin{bmatrix} 1 & v & 0 \\ v & 1 & 0 \\ 0 & 0 & \frac{1-v}{2} \end{bmatrix} \end{aligned} \tag{D.3}$$

Adopting a linear stress distribution along the thickness of the plate the moment-stress relation is

$$M_{\alpha\beta} = -\int_{-\frac{h}{2}}^{\frac{h}{2}} z\sigma_{\alpha\beta}\, dz \tag{D.4}$$

Equilibrium equations are derived by considering force equilibrium in the z direction and moment equilibrium in the x and y direction on a infinitesimally small mid-surface square [69].

$$\begin{aligned} Q_{\alpha,\alpha} &= 0 \\ M_{\alpha\beta,\beta} &= -Q_\alpha \\ M_{\alpha\beta,\alpha\beta} &= 0 \end{aligned} \tag{D.5}$$

Boundary conditions which we consider are

$$\begin{aligned} &p \; on \; A \\ &F_z \; on \; \partial A \\ &M_\alpha \; on \; \partial A \end{aligned} \tag{D.6}$$

with p a pressure load, F_z a line load and M_α a moment.

Principle of virtual work

The principle of virtual work for the plate bending element is obtained by weakening the strong form equilibrium equation $M_{\alpha\beta,\alpha\beta} = 0$ and using the first variation of the displacement w as weighting function. This leads to the Principle of Virtual Work for a single plate bending element

$$\int_A M_{\alpha\beta}\, \delta\kappa_{\alpha\beta}\, dA = \int_A p\, \delta w\, dA + \int_{\partial A} F_z\, \delta w + M_\alpha\, \delta\varphi_\alpha\, ds. \tag{D.7}$$

where the left hand side contains the internal virtual work. $\delta\kappa_{\alpha\beta}$ is work conjugate to the bending moments $M_{\alpha\beta}$. The right hand side contains the external virtual work with p a distributed pressure load, F_z a line load and M_α a moment per unit length applied on the boundary [53].

Assumed stress hybrid formulation

We follow a similar procedure as used in the derivation of the assumed stress hybrid beam element of appendix C. We add the weak form of the kinematic relations (D.2) to the virtual work formulation (D.7) by making use of the Lagrange multipliers λ_1 and λ_2 and we obtain a modification of the Principle of Virtual Work

$$\int_A M_{\alpha\beta}\, \delta\kappa_{\alpha\beta} + \lambda_1\, \delta\left(\frac{1}{2}\left(\varphi_{\alpha,\beta} + \varphi_{\beta,\alpha}\right) - \kappa_{\alpha\beta}\right) + \lambda_2 \delta\left(w_{,\alpha} - \varphi_\alpha\right)\, dA = \int_A p\, \delta w\, dA + \int_{\partial A} F_z\, \delta w + M_\alpha\, \delta\varphi_\alpha\, ds.$$

We exploit the symmetry of the change of curvature tensor κ and the Lagrange multiplier λ_1. Therefore we can write

$$\int_A \lambda_1\, \delta\left(\frac{1}{2}\left(\varphi_{\alpha,\beta} + \varphi_{\beta,\alpha}\right)\right) dA = \int_A \lambda_1\, \delta\varphi_{\alpha,\beta}$$

This can be verified by checking the physical interpretation of the kinematic relations [68].

The principle of virtual work is defined as the first variation of the potential energy functional $\delta\Pi$ [67]. A physical interpretation of the Lagrange multipliers is sought by taking the first variation of the potential energy function with respect to the curvature κ and the rotations φ

$$\begin{aligned} \delta\Pi &= \frac{\partial\Pi}{\partial\kappa}\delta\kappa = 0 \\ &\left(\int_A M_{\alpha\beta} - \lambda_1\, dA\right)\delta\kappa = 0 \\ \lambda_1 &= M_{\alpha\beta} \end{aligned}$$

by first substituting $\lambda_1 = M_{\alpha\beta}$ and $M_{\alpha\beta}\varphi_{\alpha,\beta} = \left(M_{\alpha\beta}\varphi_\alpha\right)_{,\beta} - M_{\alpha\beta,\beta}\varphi_\alpha$

$$\begin{aligned}
\delta\Pi &= \frac{\partial\Pi}{\partial\varphi}\delta\varphi = 0 \\
&\left(\int_A -M_{\alpha\beta,\beta} - \lambda_2 \, dA + \int_{\partial A} M_\alpha - M_\alpha \, ds\right) \delta\varphi = 0 \\
&\lambda_2 = -M_{\alpha\beta,\beta} \\
&\lambda_2 = Q_\alpha
\end{aligned}$$

We found an interpretation for the Lagrange multipliers, respectively the bending moments $M_{\alpha\beta}$ and the transverse shear force Q_α. We proceed with the derivation by substituting the interpretation. We denote the external virtual work with W. We find

$$\int_A M_{\alpha\beta}\,\delta\kappa + M_{\alpha\beta}\,\delta\varphi_{\alpha,\beta} - M_{\alpha\beta}\,\kappa + Q_\alpha\,\delta w_{,\alpha} - Q_\alpha\,\delta\varphi_\alpha\,dA = W$$

Now we substitute the equilibrium equation $Q_\alpha = -M_{\alpha\beta,\beta}$ to exclude the transverse shear force from the virtual work equation. The result is

$$\int_A M_{\alpha\beta}\,\delta\varphi_{\alpha,\beta} - M_{\alpha\beta,\beta}\,\delta w_{,\alpha} + M_{\alpha\beta,\beta}\,\delta\varphi_\alpha\,dA = W$$

By using the product rule $M_{\alpha\beta,\beta}\varphi_\alpha + M_{\alpha\beta}\varphi_{\alpha,\beta} = (M_{\alpha\beta}\varphi_\alpha)_{,\beta}$ and divergence theorem we combine two terms and bring the resulting term to the boundary integral

$$\int_A -M_{\alpha\beta,\beta}\,\delta w_{,\alpha}\,dA + \int_{\partial A} M_{\alpha\beta}\varphi_\alpha n_\alpha\,ds = W$$

Now we use the product rule $-M_{\alpha\beta,\beta}\delta w_{,\alpha} = M_{\alpha\beta,\alpha\beta}\delta w - (M_{\alpha\beta,\beta}\delta w)_{,\alpha}$ and divergence theorem again. Arriving at the simplified expression for virtual work for a single element

$$\int_A M_{\alpha\beta,\alpha\beta}\,\delta w\,dA + \int_{\partial A} M_{\alpha\beta}\delta\varphi_\alpha\,n_\alpha - M_{\alpha\beta,\beta}\delta w\,n_\alpha\,ds = W \tag{D.8}$$

Discretization

In this paragraph the finite element equations will be derived by introducing a discretization into the final virtual work expression (D.8).

A primary variable is a variable which is connected to a physical quantity which are used in the virtual work equation (D.8). The primary variables are the bending moments $M_{\alpha\beta}$, the rotations φ_α and the transverse displacements w. m are called generalized stresses and are related to the bending moments by a constant interpolation, as follows

$$m = \begin{bmatrix} M_{11} & M_{22} & M_{12} \end{bmatrix}^T$$

Three independent generalized stresses are defined corresponding to three generalized strains. This means that three deformation modes are present. The element has three rigid body modes. Therefore the $KL0$ element should have six independent kinematic degrees of freedom, three translations and three rotations, to correctly formulate the element, see Figure D.2. By correctly formulating the element, no spurious energy modes or locking phenomena are present. This means for example that for the rigid body modes no strain energy is developed by the element.

Because the $KL0$ element assumes constant bending moments, $M_{\alpha\beta,\alpha\beta} = 0$ (equation of equilibrium) is always satisfied. The area integral term in the internal virtual work expression is therefore also satisfied $\int_A M_{\alpha\beta,\alpha\beta}\,dA = 0$. Only boundary integral terms in the virtual work expression remains. This means that only interpolations for the transverse displacements w and the rotation φ along the boundaries of the element have to be defined.

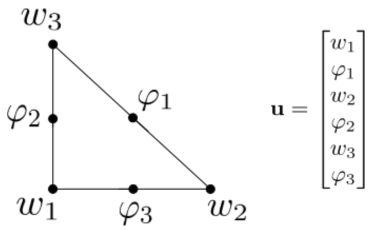
w_3
φ_2
φ_1
w_1
φ_3
w_2
$\mathbf{u} = \begin{bmatrix} w_1 \\ \varphi_1 \\ w_2 \\ \varphi_2 \\ w_3 \\ \varphi_3 \end{bmatrix}$

Figure D.2: Definitions of DOF at plate bending element

The rotations along the element sides φ_n^i with $i = 1, 2, 3$ are taken constant

$$\varphi_n^i = \begin{bmatrix} -\varphi_1 \\ -\varphi_2 \\ -\varphi_3 \end{bmatrix}$$

A linear interpolation of the transverse displacements is introduces along the boundaries of the element

$$w^i = \begin{bmatrix} 1 - \xi & \xi \end{bmatrix} \begin{bmatrix} w_{begin} \\ w_{end} \end{bmatrix}$$

with

$$\xi_i = \frac{s_i}{\lambda_i}$$

The constitutive relation should connect the generalized stress m with the generalized strain κ, how are work conjugates. The constitutive relations are evaluated in the material sampling point which is located in the center of the element. The generalized stresses in the material sampling point is denoted as m_s and can be found by $m_s = I_3\, m$, with I_3 a 3x3 identity matrix. The generalized strains are denoted as κ and are found by observing the expression for virtual work. Evaluating the virtual work expression by sampling in the material sampling point gives

$$\int_A M_{\alpha\beta}\, \delta\kappa_{\alpha\beta}\, dA = A\, m_s\, \delta\kappa_s = A\, I_3\, m\, \delta\kappa_s$$

Observing the equation for virtual work the expression for the generalized strains κ is found

$$\kappa = A\, I_3\, \kappa_s$$

Now the constitutive relation between the generalized stresses and strains can be found. The constitutive relation is evaluated in the material sampling points and read

$$m_s = E_b\, \kappa_s$$

with

$$E_b = \frac{E h^3}{12(1 - v^2)} \begin{bmatrix} 1 & v & 0 \\ v & 1 & 0 \\ 0 & 0 & \frac{1-v}{2} \end{bmatrix}$$

Rewriting the above constitutive relation in terms of the generalized stresses and strains give

$$m = S_b\, \kappa$$

with

$$S_b = \frac{E_b}{A}$$

Now the interpolations are introduced into the virtual work expression (D.8). Per term I would like to present a derivation as an example. The goal is to formulate the virtual work expression in discrete matrix form.

Starting with the area term, which is always zero for constant bending moments

$$\int_A M_{\alpha\beta,\alpha\beta} \delta w \, dA = 0$$

Before proceeding the coordinate system of the final expression for virtual work is changed from the global coordinate system to the coordinate systems associated with the element sides. Recall that per element side a tangential and a normal base vector is defined, corresponding to subscripts (s, n). Note that the in-plane tensors in the global coordinate system are decomposed into two contributions in the coordinate system of the element sides. This results in

$$\int_{\partial A} M_{nn} \delta\varphi_n + M_{ns} \delta w_{,s} - M_{nn,n} \delta w - M_{ns,s} \delta w \, ds = \int_A p \delta w \, dA + \int_{\partial A} F_z \delta w + M_n \delta\varphi_n + M_s \delta w_{,s} \, ds$$

with

$$\varphi_s = w_{,s}$$

One boundary term is including the moment around the sides M_{nn} of the element. This is paired with the rotations around the sides φ_n how are work conjugates. This term can be interpreted as the term which ensures continuity of the bending moments over the element boundaries. This term is written in discretized matrix form using the coordinate transformation (D.1) as

$$\sum_{i=1}^{3} \int_0^{\lambda_i} M^i_{nn} \delta\varphi^i_n \, ds_i = \mathbf{m}^T \mathbf{D}_\varphi \delta\varphi$$

The boundary term corresponding to the transverse displacements is treated here, the product rule $M^i_{ns} \delta w^i_{,s} = M_{ns,s} \delta w - (M_{ns} \delta w)_{,s}$ and divergence theorem are used to simplify the expression.

$$\sum_{i=0}^{3} \int_0^{\lambda_i} M^i_{ns} \delta w^i_{,s} - \left(M^i_{nn,n} + M^i_{ns,s}\right) \delta w^i \, ds_i$$

$$\sum_{i=0}^{3} \int_0^{\lambda_i} -M_{nn,n} \delta w \, ds_i - \left[M^i_{ns} \delta w\right]_0^{\lambda_i}$$

resulting in

$$\sum_{i=0}^{3} \left[M^i_{ns} \delta w^i\right]_0^{\lambda_i} = \mathbf{m}^T \mathbf{D}_w \delta \mathbf{w} \tag{D.9}$$

The left hand side of (D.9) is continuous and the right hand side is discrete. Here we illustrate for one side $i = 1$ how we derive matrix $\mathbf{D}_w$ using the coordinate transformation (D.1) and the interpolation for w.

$$M^1_{ns} = \frac{1}{\lambda_1^2} - b_1 \left(a_1 M_{11} - b_1 M_{12}\right) - a_1 \left(a_1 M_{21} - b_1 M_{22}\right)$$

$$\delta w = \left[\begin{bmatrix} 1 - \xi & \xi \end{bmatrix} \delta \begin{bmatrix} w_2 \\ w_3 \end{bmatrix}\right]_0^{\lambda_1}$$

$$\delta w = w_3 - w_2$$

Substitution of $M^1_{ns}]$ into the left hand side of (D.9) leads to the following equation. Note that there is another contribution for δw_3 to matrix $\mathbf{D}_w$ which is not shown here.

$$\begin{bmatrix} M_{11} & M_{22} & M_{12} \end{bmatrix} \begin{bmatrix} -b_1 a_1 / \lambda_1^2 \\ b_1 a_1 / \lambda_1^2 \\ b_1^2 / \lambda_1^2 - a_1^2 / \lambda_1^2 \end{bmatrix} \delta w_3$$

Now the terms corresponding to the external virtual work will be evaluated. Starting with the pressure term. The pressure is assumed to be constant throughout the element and are introduced as work equivalent nodal forces

$$\int_A p\delta w\, dA = \frac{pA}{3}\begin{bmatrix}1\\1\\1\end{bmatrix}\delta\mathbf{w}$$

The moment loading around the sides are introduced as

$$\sum_{i=1}^{3}\int_0^{\lambda_i} M_n^i\delta\varphi_n^i\, ds_i = \begin{bmatrix}\lambda_1 M_1 & \lambda_2 M_2 & \lambda_3 M_3\end{bmatrix}\delta\varphi$$

The distributed line loading is introduced as follows. The line load is assumed constant over de element side, therefore the contribution from M_s is zero. Here we write out the contribution of one side.

$$\sum_{i=1}^{3}\int_0^{\lambda_i} F^i\delta w^i\, ds_i = \mathbf{F}\delta\mathbf{w}$$

$$\int_0^{\lambda_1} F^1\delta\begin{bmatrix}1-\frac{s}{\lambda_1} & \frac{s}{\lambda_1}\end{bmatrix}\begin{bmatrix}w_2\\w_3\end{bmatrix} ds_1 = \frac{1}{2}\lambda_1 F^1\delta w_2 + \frac{1}{2}\lambda_1 F^1\delta w_3$$

Finally we would like to show the derivation of the stiffness matrix for the $KL0$ plate bending element, by substituting the discrete terms which are found above into the virtual work equation we find

$$m^T\left[D_w\delta w + D_\varphi\delta\varphi\right] = F\delta w + M\delta\varphi$$

The right hand side of aboves equation gives us the expression for the generalized deformations κ because these need to be work conjugates to the generalized stresses m and herewith the strain-nodal displacement relation is found $\kappa = D_w w + D_\varphi\varphi$. Substituting the constitutive and strain-displacement relation into aboves expression gives us the expression for the stiffness matrix

$$\begin{bmatrix}D_w^T\\D_\varphi^T\end{bmatrix} S\begin{bmatrix}D_w & D_\varphi\end{bmatrix}\begin{bmatrix}w\\\varphi\end{bmatrix} = \begin{bmatrix}F\\M\end{bmatrix}$$

Numerical examples

The $KL0$ element is derived in the preceding section. In this paragraph the element is compared with the exact solution for three load cases, a moment, a distributed line load and a distributed pressure load. Two different square meshes of unit length are used, shown in Figure D.3. Linear elastic material behaviour with a Poisson's ratio of $v = 0.3$ is used. The boundary conditions for both meshes are the same and read:

- A and C: $\varphi_n = 0$
- B: Moment or line load
- D: $\varphi_n = 0$ and $w = 0$
- Area: distributed pressure

The moment load applied on the example meshes result in a constant bending moment and zero transverse shear throughout the plate. The $KL0$ element exhibit constant bending moments and should therefore be able to approximate the deformation of a plate, loaded by a moment, exactly. The exact solution for a moment load is

$$w_e = \frac{1}{D}\frac{1}{2}ML^2$$

$$\varphi_e = \frac{1}{D}ML$$

with

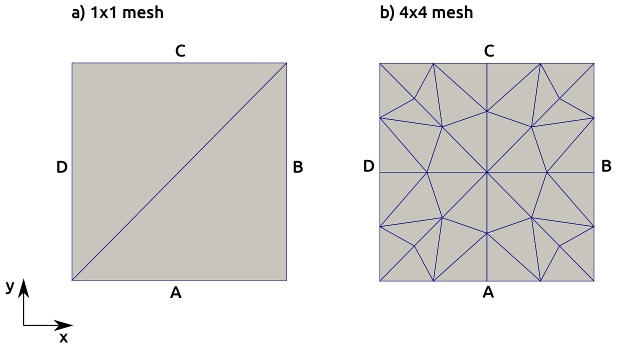

Figure D.3: Meshes for numerical tests

$$D = \frac{Eh^3}{12(1-v^2)}$$

A plate loaded by a distributed line load results in a linear bending moment and constant transverse shear forces within the plate. Therefore the $KL0$ element is not able give an exact solution for a distributed line load. The exact solution of a line load is

$$w_e = \frac{1}{D}\frac{1}{3}FL^3$$
$$\varphi_e = \frac{1}{D}\frac{1}{2}FL^2$$

For a distributed pressure loading the exact bending moment varies quadratically within the plate. The transverse shear forces vary linearly. The element cannot give an exact solution for a pressure load. The exact solution for a distributed pressure load is

$$w_e = \frac{1}{D}\frac{1}{8}pL^4$$
$$\varphi_e = \frac{1}{D}\frac{1}{6}pL^3$$

Tables D.1, D.2, D.3 and D.4 show the results of the $KL0$ element in hybrida compared with the results of the same element reported by van Keulen [53]. A thickness ratio of 1% and 20% is used for the analysis. The values is the column w_{norm} present the averaged transverse displacements of the side $x = L$ which are normalized by the exact solution. Similarly, column φ_{norm} presents the average rotations about side $x = L$ normalized by the exact solution. The error values Δw and $\Delta\varphi$ are defined by

$$\Delta w = \left[\frac{max(|w|) - |w_e|}{|w_e|}\right]_{x=L}$$
$$\Delta\varphi = \left[\frac{max(|\varphi|) - |\varphi_e|}{|\varphi_e|}\right]_{x=L}$$

Table D.1: Plate loaded by a distributed line load with 1 % thickness

$KL0$ element by	Mesh	w_{norm}	Δw	φ_{norm}	$\Delta\varphi$
hybrida	1x1	2.07	115 %	1.00	0.0 %
	4x4	1.05	5.2 %	1.00	1.4 %
van Keulen [53]	1x1	2.07	114	1.00	0.0
	4x4	1.06	6	1.00	1.3

Table D.2: Plate loaded by a distributed pressure load with 1 % thickness

$KL0$ element by	Mesh	w_{norm}	Δw	φ_{norm}	$\Delta\varphi$
hybrida	1x1	2.72	178 %	1.50	50 %
	4x4	1.08	8 %	1.03	3 %
van Keulen [53]	1x1	2.71	178	1.50	50
	4x4	1.09	9	1.03	4

Table D.3: Plate loaded by a distributed line load with 20 % thickness

$KL0$ element by	Mesh	w_{norm}	Δw	φ_{norm}	$\Delta\varphi$
hybrida	1x1	2.07	115 %	1.00	0.0 %
	4x4	1.05	5.2 %	1.00	1.4 %
van Keulen [53]	1x1	2.07	115 %	1.00	0.0 %
	4x4	1.06	6 %	1.00	1.3 %

It is confirmed that the $KL0$ element implemented in hybrida gives exact solution for moment loadings. For the line loading an error is observed which decreases when the mesh is refined. For the pressure load the error is slightly higher. The values compare well with the results by van Keulen [53].

Table D.4: Plate loaded by a distributed pressure load with 20 % thickness

$KL0$ element by	Mesh	w_{norm}	Δw	φ_{norm}	$\Delta\varphi$
hybrida	1x1	2.72	178 %	1.50	50 %
	4x4	1.08	8 %	1.03	3 %
van Keulen [53]	1x1	2.72	178 %	1.50	50 %
	4x4	1.09	9 %	1.03	3 %

E

Consistent finite rotation shell elements

In this appendix a triangular shell element will be described which is based on the constant moment plate bending element $KL0$ developed in appendix D. The plate bending element is combined with a Constant Stain Triangle (CST) which results in a triangular shell element with three translational DOFs per node and one rotational DOF per side (12 DOFs per element). The element will not take initial curvature into account and is therefore denoted as a Facet element. The element adopts a finite rotation (FR) formulation to calculate the changes of curvature κ. This element is named $F0d - FR$. The formulation of this element follows the procedure described by van Keulen [53]. This element is advanced by implementing a consistent tangent operator for the shell element and this element is named $F0d - FR - C$. This is done according to the work of Booij and van Keulen [54]. In this appendix, several derivations are given, but it is recognized that it is not complete. For a complete derivation, one should see the references given above.

First the membrane part of the element is presented. In combination with the bending part of appendix D and a finite rotation formulation this will result in the finite rotation shell element $F0d - FR$. Then the derivation of the consistent tangent operator will be given. This results in the $F0d - FR - C$ element. Finally, several numerical examples will be described.

Facet element

The facet element described here is capable of simulating finite rotations and displacements, but is restricted to small strains. The formulation for the chances of curvature is based on a finite rotation formulation. The limitations of the element are noted here. First of all, the Kirchoff-Love plate bending element $KL0$ does not take transverse shear deformation into account. Furthermore, the constant membrane and bending stress states within the elements can lead to bad approximations of the actual stresses in regions with stress concentrations. As long as the thickness is relatively thin and the stress gradients are small the element is expected to perform well. Furthermore, the approximation of curved geometries with the facet element can introduce numerical errors.

Membrane strain

Membrane strains are determined by starting from the non-linear Lagrange strain γ and interpolating the nodal displacements linearly. γ represents the mid-surface in-plane strain associated with the element in-plane coordinate system (x_α, n)

$$\gamma_{\alpha\beta} = \frac{1}{2}\left(u_{\alpha,\beta} + u_{\beta,\alpha} + u_{i,\alpha}u_{i,\beta}\right)$$

with

$$\alpha, \beta = 1, 2$$
$$i = 1, 2, 3$$

Area coordinates are used to perform the linear interpolation from the nodal displacements to a continuous displacement field [53, 70]

$$\begin{aligned} u_1(\chi_1,\chi_2,\chi_3) &= \chi_1 u_1 + \chi_2 u_2 + \chi_3 u_3 \\ u_2(\chi_1,\chi_2,\chi_3) &= \chi_1 v_1 + \chi_2 v_2 + \chi_3 v_3 \\ u_3(\chi_1,\chi_2,\chi_3) &= \chi_1 w_1 + \chi_2 w_2 + \chi_3 w_3 \end{aligned}$$

with A_i the area fractions of the triangle

$$\chi_i = \frac{A_i}{A}$$
$$i = 1,2,3$$

Derivatives of the variables which dependent on an area coordinate χ can be determined as follows

$$\begin{aligned} u_{1,1} &= \frac{b_i}{2A}\frac{\partial u_1}{\partial \chi_i} & u_{1,2} &= \frac{a_i}{2A}\frac{\partial u_1}{\partial \chi_i} \\ u_{2,1} &= \frac{b_i}{2A}\frac{\partial u_2}{\partial \chi_i} & u_{2,2} &= \frac{a_i}{2A}\frac{\partial u_2}{\partial \chi_i} \\ u_{3,1} &= \frac{b_i}{2A}\frac{\partial u_3}{\partial \chi_i} & u_{3,2} &= \frac{a_i}{2A}\frac{\partial u_3}{\partial \chi_i} \\ i &= 1,2,3 \end{aligned}$$

and

$$\begin{aligned} \frac{\partial u_1}{\partial \chi_i} &= u_i \\ \frac{\partial u_2}{\partial \chi_i} &= v_i \\ \frac{\partial u_3}{\partial \chi_i} &= w_i \\ i &= 1,2,3 \end{aligned}$$

We used the proposed expressions to write out and simplify the expression for the membrane strain tensor γ in terms of the nodal displacements u, v, w.

$$\begin{aligned} \gamma_{11} &= \frac{1}{2}\left(u_{1,1} + u_{1,1} + u_{1,1}u_{1,1} + u_{2,1}u_{2,1} + u_{3,1}u_{3,1}\right) \\ \gamma_{22} &= \frac{1}{2}\left(u_{2,2} + u_{2,2} + u_{1,2}u_{1,2} + u_{2,2}u_{2,2} + u_{3,2}u_{3,2}\right) \\ \gamma_{12} &= \frac{1}{2}\left(u_{1,2} + u_{2,1} + u_{1,1}u_{1,2} + u_{2,1}u_{2,2} + u_{3,1}u_{3,2}\right) \end{aligned}$$

Writing out term $u_{1,1}u_{1,1}$ of γ_{11} gives

$$u_{1,1}u_{1,1} = \left(\frac{b_1}{2A}u_1 + \frac{b_2}{2A}u_2 + \frac{b_3}{2A}u_3\right)\left(\frac{b_1}{2A}u_1 + \frac{b_2}{2A}u_2 + \frac{b_3}{2A}u_3\right)$$

$$u_{1,1}u_{1,1} = \begin{bmatrix} u_1 & u_2 & u_3 \end{bmatrix} \frac{1}{4A^2} \begin{bmatrix} b_1^2 & b_1 b_2 & b_1 b_3 \\ b_2 b_1 & b_2^2 & b_2 b_3 \\ b_3 b_1 & b_3 b_2 & b_3^2 \end{bmatrix} \begin{bmatrix} u_1 \\ u_2 \\ u_3 \end{bmatrix}$$

Performing this for all terms results in the membrane strain vector, in Voight notation, $\varepsilon_m = \begin{bmatrix} \gamma_{11} & \gamma_{22} & 2\gamma_{12} \end{bmatrix}^T$ and

$$\varepsilon_m = \begin{bmatrix} d_1 u + \frac{1}{2}\left(u^T c_1 u + v^T c_1 v + w^T c_1 w\right) \\ d_2 v + \frac{1}{2}\left(u^T c_2 u + v^T c_2 v + w^T c_2 w\right) \\ d_2 u + d_1 v + \frac{1}{2}\left(u^T c_3 u + v^T c_3 v + w^T c_3 w\right) \end{bmatrix}$$

with

$$d_1 = \frac{1}{2A}\begin{bmatrix} b_1 & b_2 & b_3 \end{bmatrix} \quad d_2 = \frac{1}{2A}\begin{bmatrix} a_1 & a_2 & a_3 \end{bmatrix}$$

$$c_1 = \frac{1}{4a^2}\begin{bmatrix} b_1^2 & b_1 b_2 & b_1 b_3 \\ b_2 b_1 & b_2^2 & b_2 b_3 \\ b_3 b_1 & b_3 b_2 & b_3^2 \end{bmatrix} \quad c_2 = \frac{1}{4a^2}\begin{bmatrix} a_1^2 & a_1 a_2 & a_1 a_3 \\ a_2 a_1 & a_2^2 & a_2 a_3 \\ a_3 a_1 & a_3 a_2 & a_3^2 \end{bmatrix}$$

$$c_3 = \frac{2}{4a^2}\begin{bmatrix} b_1 a_1 & b_1 a_2 & b_1 a_3 \\ b_2 a_1 & b_2 a_2 & b_2 a_3 \\ b_3 a_1 & b_3 a_2 & b_3 a_3 \end{bmatrix}$$

Generalized membrane force
We found the membrane strain vector ε_m. We would like to continue deriving a constitutive relation connecting the generalized membrane strains to the generalized membrane forces who are work conjugates. The constitutive relations are evaluated in the material sampling point as well as the sampling of the virtual work equation from continuous to discrete. By observing the virtual work expression we can find an expression for the generalized membrane stress σ_m (also called the generalized membrane force) in terms of the generalized membrane strain ε_m.

$$\gamma_s = I_3\, \varepsilon_m$$

$$\int_A N_{\alpha\beta}\delta\gamma_{\alpha\beta}\, dA = A\, N_s\, \delta\gamma_s = A\, N_s\, I_3\, \delta\varepsilon_m$$

$$\sigma_m = A\, N_s\, I_3$$

with

$$\gamma_s = \begin{bmatrix} \gamma_{11}^s & \gamma_{22}^s & 2\gamma_{12}^s \end{bmatrix}^T$$

$$N_s = \begin{bmatrix} N_{11}^s & N_{22}^s & N_{12}^s \end{bmatrix}^T$$

The constitutive relation is evaluated in the material sampling points and read

$$N_s = E_{mm}\, \gamma_{mm}$$

with

$$E_{mm} = \frac{Eh}{1-v^2}\begin{bmatrix} 1 & v & 0 \\ v & 1 & 0 \\ 0 & 0 & \frac{1-v}{2} \end{bmatrix}$$

The constitutive relation connecting the generalized strains and stresses is derived and shown here

$$\sigma_m = S_{mm}\, \varepsilon_m$$

with

$$S_{mm} = A\, E_{mm}$$

Combining membrane and bending components
Here we will combine the membrane part of the element, derived in the preceding paragraph with the plate bending element of appendix D. This is possible since the DOFs of both elements are independent for a symmetrically layered shell.

The nodal-displacement vector U, the combined generalized stresses σ and the combined generalized strains ε, material matrix S (restricted to linear elastic material) and the combined force vector F are defined by

$$U = \begin{bmatrix} u_1 & u_2 & u_3 & v_1 & v_2 & v_3 & w_1 & w_2 & w_3 & \varphi_1 & \varphi_2 & \varphi_3 \end{bmatrix}^T$$

$$\sigma = \begin{bmatrix} \sigma_m \\ \sigma_b \end{bmatrix}$$

$$\varepsilon = \begin{bmatrix} \varepsilon_m \\ \varepsilon_b \end{bmatrix}$$

$$S = \begin{bmatrix} S_m & 0_{3x3} \\ 0_{3x3} & S_b \end{bmatrix}$$

$$F = \begin{bmatrix} Fu_1 & Fu_2 & Fu_3 & Fv_1 & Fv_2 & Fv_3 & Fw_1 & Fw_2 & Fw_3 & M_1 & M_2 & M_3 \end{bmatrix}^T$$

We would like to assemble the contribution of the membrane strains and the changes of curvature to the combined strain-displacement matrix valid for large rotations. For the membrane strains this is straight forward since these are already valid for finite displacements and rotations. To extent the definition of the changes of curvature (generalized bending stresses) to large rotations, rate equations are formulated as follows

$$\kappa = D_w w + D_\varphi \varphi$$
$$\dot{\kappa} = D_w \dot{w} + D_\varphi \dot{\varphi}$$

with

$$\dot{w} = n_1 \dot{u} + n_2 \dot{v} + n_3 \dot{w}$$

substitution yields

$$\dot{\kappa} = n_1 D_w \dot{u} + n_2 D_w \dot{v} + n_3 D_w \dot{w} + D_\varphi \dot{\varphi}$$

The above expressions are used to combine the discrete strain-displacement relation for the membrane part and bending part into the combined strain-displacement matrix D

$$D = \begin{bmatrix} d_1 + u^T c_1 & v^T c_1 & w^T c_1 & 0_{1x3} \\ u^T c_2 & d_2 + v^T c_2 & w^T c_2 & 0_{1x3} \\ d_2 + u^T c_3 & d_1 + v^T c_3 & w^T c_3 & 0_{1x3} \\ n_1 D_w & n_2 D_w & n_3 D_w & D_\varphi \end{bmatrix}$$

Finite rotation formulation

The derivation for the membrane part as shown above is valid for finite rotations and displacements. For the bending part the generalized bending strain ε_b or also known as the changes of curvature κ are reconsidered to make them valid for finite rotation and displacements. The idea behind this is that bending of an element should be evaluated independently from the rigid body rotation of that element. In the linear regime, considered in appendix D, the changes of curvature κ were evaluated using actual nodal displacements and rotations. This was possible since the rotations and displacements were assumed small. To calculate the changes of curvature while the element is subjected to large rotations we should subtract the rigid body rotation from the actual displacements and rotations of the element. These are called relative displacements and rotations. The changes of curvature can be evaluated in the same way as described in the preceding chapter but are now depending on relative displacements $\tilde{w}$ and rotations $\tilde{\varphi}$, shown here

$$\varepsilon_b = D_w \tilde{w} + D_\varphi \tilde{\varphi}$$

The question is how the relative rotations $\tilde{\varphi}$ should be determined. When the relative rotations are found, the calculation of the changes of curvature will be straight forward $\kappa = D_\varphi \tilde{\varphi}$. To find the relative rotations $\tilde{\varphi}$ we will follow the approach developed by van Keulen in Chapter 5 [53] and the article of Booij and van Keulen [54]. A summary will be given here.

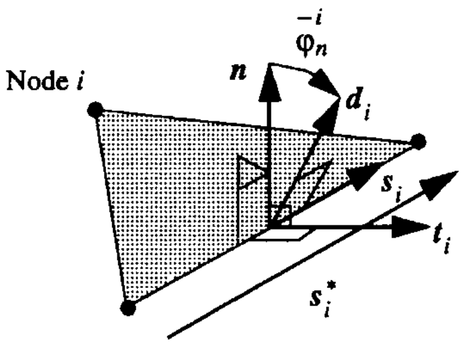

Figure E.1: Overview of vectors [54]

To determine the new bending strain ε_b several vectors per element side are used to differentiate between the deformation of the element due a rigid rotation and deformation due to bending of the element. These vectors are associated to the Corotated Reference Triangle. In a deformed configuration this reference triangle is defined by the corner nodes. In the initial configurations the Initial Reference Triangle and the Corotated Reference Triangle are the same.

First of all vector $\tilde{s}$ along the sides of the CRT, the vector $\tilde{t}$ normal to the CRT sides, the reference vector $\tilde{r}$, the normal to the CRT surface n and the directors $\tilde{d}$, are introduced see Figure E.1.

For every side applies

$$\tilde{s} \cdot \tilde{d} = 0$$
$$\tilde{s} \cdot \tilde{t} = 0$$

A redefinition to calculate the bending strain ε_b is given. We adopt the definition given in [54].

$$\tilde{\varphi}_i = \arctan\left(\frac{\tilde{t}_i \cdot \tilde{d}_i}{n \cdot \tilde{d}_i}\right)$$
$$\varepsilon_b = D_\varphi \, \tilde{\varphi}$$

The question remains how the director is calculated. The director is a measure of the bending of the shell excluding the rigid body rotations. To calculate the director the reference vector r is updated every iteration by the directional change of the corresponding side. Therefore the reference vector r functions as a representation of the rigid body rotations.

$$r^{k+1} = T\, r^k$$

The directors per element and per element side are calculated in the following way

$$d = r\cos(\varphi) + (s \times r)\sin(\varphi)$$

Finite element equations

Starting out from the discrete virtual work expression and using the combined vectors as defined above, we derive the non-linear finite element equations. The discrete virtual work expression reads

$$\sigma\, \delta\varepsilon = F\, \delta U$$

Substituting

$$\delta\varepsilon = D\delta U$$

gives

$$\sigma\, D = F$$

In the above equation D and σ are depending on u therefore we define rate equations to be able to solve the system using a non-linear solution method. Differentiation with respect to a pseudo time and substitution of $\dot{\sigma} = S\,D\,\dot{U}$ is applied

$$\begin{aligned} &D^T\dot{\sigma} + \dot{D}^T\sigma = \dot{F} \\ &D^T\,S\,D\,\dot{U} + \dot{D}^T\,\sigma = \dot{F} \\ &\left(D^T\,S\,D + \frac{\partial D^T}{\partial U}\,\sigma\right)\dot{U} = \dot{F} \end{aligned}$$

with

$$\begin{aligned} K_m &= D^T\,S\,D \\ K_g &= \frac{\partial D^T}{\partial U}\,\sigma \end{aligned} \tag{E.1}$$

Finally we would like to discus the geometric stiffness matrix K_g in more detail. In this section we assume that K_g is depending on the membrane stresses σ_m only. For small rotations this assumption is satisfactory, but in this case, were we consider finite rotations this assumption results in an inconsistent stiffness matrix.

We use the nodal displacement vector in the form $U = \begin{bmatrix} u & v & w \end{bmatrix}$ and the membrane stress components σ_m while working out the expression for the geometric stiffness matrix K_g. We use the index notation, as was used in [54]. We use G instead of K_g and write D as $\frac{\partial \varepsilon}{\partial U}$

$$G_{ij} = \frac{\varepsilon_k}{\partial U_i \partial U_j}\sigma_k \tag{E.2}$$

To illustrate the principle we write out the term G_{11}

$$\begin{aligned} G_{11} &= \frac{\partial^2 \varepsilon_1}{\partial U_1 \partial U_1}\sigma_1 + \frac{\partial^2 \varepsilon_2}{\partial U_1 \partial U_1}\sigma_2 + \frac{\partial^2 \varepsilon_3}{\partial U_1 \partial U_1}\sigma_3 \\ G_{11} &= \frac{1}{4A^2}\begin{bmatrix} b_1^2 & a_1^2 & b_1 a_1 \end{bmatrix}\begin{bmatrix} \sigma_1 \\ \sigma_2 \\ \sigma_3 \end{bmatrix} \end{aligned} \tag{E.3}$$

Deriving a consistent tangent operator

For the derivation of the consistent tangent operator we followed the derivation as given by Bout and van Keulen [54]. In this paragraph I would like to show several derivations to illustrate the principles involved. Furthermore, my intention is to give backround information and a broader explanation of the implementation described by the article of Booij and van Keulen.

The element with consistent tangent operator differs by two parts. The first is a change in the strain-displacement matrix D for the bending part. Second part will be a change will be an addition to the geometric stiffness matrix which will now not only depend on the membrane stress but also on the bending stress.

As mentioned before, the changes of curvature κ are defined by $\kappa = D_\varphi \tilde{\varphi}$ where $\tilde{\varphi}$ are the relative rotations. The relative rotations are determined by the method described above, involving the updating of the reference vectors and directors and the value of the actual rotational DOFs.

I would like to show the expression of the stiffness matrix, were B is a vector with the generalized strains. It is clear that a consistent K matrix requires first- and second order variations of the generalized deformations.

$$K = \delta_1 B^T\,S\,\delta_1 B + \sigma\delta_1\delta_2 B \tag{E.4}$$

We will concentrate on finding the first and second order variations for the bending strains. For demonstration purposes we will shown several derivations. Starting point is, following from the above expression for the K matrix

$$\begin{aligned}\delta_1\kappa &= D_\varphi\delta_1\,\tilde{\varphi}\\ \delta_1\delta_2\kappa &= D_\varphi\delta_1\delta_2\,\tilde{\varphi}\end{aligned} \tag{E.5}$$

First the above expression will be worked out further, using standard differentiation and because t, d and n are unit vectors we can say that $(t_i\cdot d_i)^2+(t_i\cdot d_i)^2=1$

$$\begin{aligned}\delta_1\tilde{\varphi} &= \delta_1\arctan\left(\frac{t_i\cdot d_i}{n\cdot d_i}\right)\\ &= \frac{1}{1+\left(\frac{t_i\cdot d_i}{n\cdot d_i}\right)^2}\cdot\delta_1\frac{t_i\cdot d_i}{n\cdot d_i}\\ &= \frac{1}{1+\left(\frac{t_i\cdot d_i}{n\cdot d_i}\right)^2}\cdot\frac{(n\cdot d_i)\,\delta_1(t_i\cdot d_i)-(t_i\cdot d_i)\,\delta_1(n\cdot d_i)}{(n\cdot d_i)^2}\\ &= (n\cdot d_i)\,\delta_1(t_i\cdot d_i)-(t_i\cdot d_i)\,\delta_1(n\cdot d_i)\end{aligned} \tag{E.6}$$

and, by product rule

$$\begin{aligned}\delta_1\delta_2\tilde{\varphi} = {}&\delta_1(t_i\cdot d_i)\delta_2(n\cdot d_i)+(n\cdot d_i)\delta_1\delta_2(t_i\cdot d_i)\\ &-\delta_1(n\cdot d_i)\delta_2(t_i\cdot d_i)+(t_i\cdot d_i)\delta_1\delta_2(n\cdot d_i)\end{aligned} \tag{E.7}$$

The above expressions for the first and second order variations of the relative rotations $\tilde{\varphi}$ form the basis for several simplifications to obtain a more compact formulation. These simplifications are well documented in [54]. Observing the above expressions and the dependencies of its components we see that the following first and second order variations of vectors should be evaluated

$$\begin{array}{ll}\delta_1 t_i & \delta_1\delta_2 t_i\\ \delta_1 n & \delta_1\delta_2 n\\ \delta_1 d_i & \delta_1\delta_2 d_i\\ \delta_1 s_i & \delta_1\delta_2 s_i\\ \delta_1 r_i & \delta_1\delta_2 r_i\end{array} \tag{E.8}$$

Solution procedures

Clearly, a non-linear solution procedure should be used to solve the non-linear finite element equations. A standard Newton-Rapshon solution procedure is used. By Leon *et al.*, a unified solution procedure is proposed [57]. In this unified approach the load and arc-length control algorithms are described in detail.

Numerical examples

Three example problems are calculated to compare the performance of the elements $F0d-FR$ and $F0d-FR-C$, respectively the non consistent and the consistent one. First the pure bending of a strip into a cylinder is presented. Thereafter the hemispherical shell problem is described. Both test examples are well known benchmark problems. Finally we present the cylindrical roof exhibiting snap-back behaviour to demonstrate the performance of the elements beyond limit points in the load and displacement.

Pure bending of a strip

A strip with length L and thickness h is bend by a moment into a cylinder. The moment to bend the strip in an exact cylinder is calculated by

$$M=\frac{Eh^3}{12(1-\nu^2)}\frac{2\pi}{L} \tag{E.9}$$

A Poisson's ratio of 0.3 and a thickness to width ratio of 1% is used. Symmetry boundary conditions are used for the bottom and top 'long' edges. One 'short' edges is clammed and one is loaded by the moment M. A regular mesh is used. Figure E.2 shows the deformed and undeformed configurations.

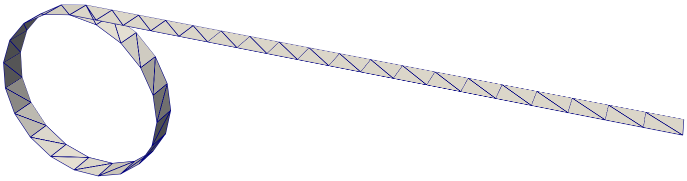

Figure E.2: Bending of a strip into a cylinder

A Newton-Rapshon load control is used with a force norm of $1 \cdot 10^{-4}$ as convergence criteria. Two load cases are simulated one with 10 load steps and one with a single load step. For comparison I add the force remainder plots from Bout and van Keulen for this problem [54].

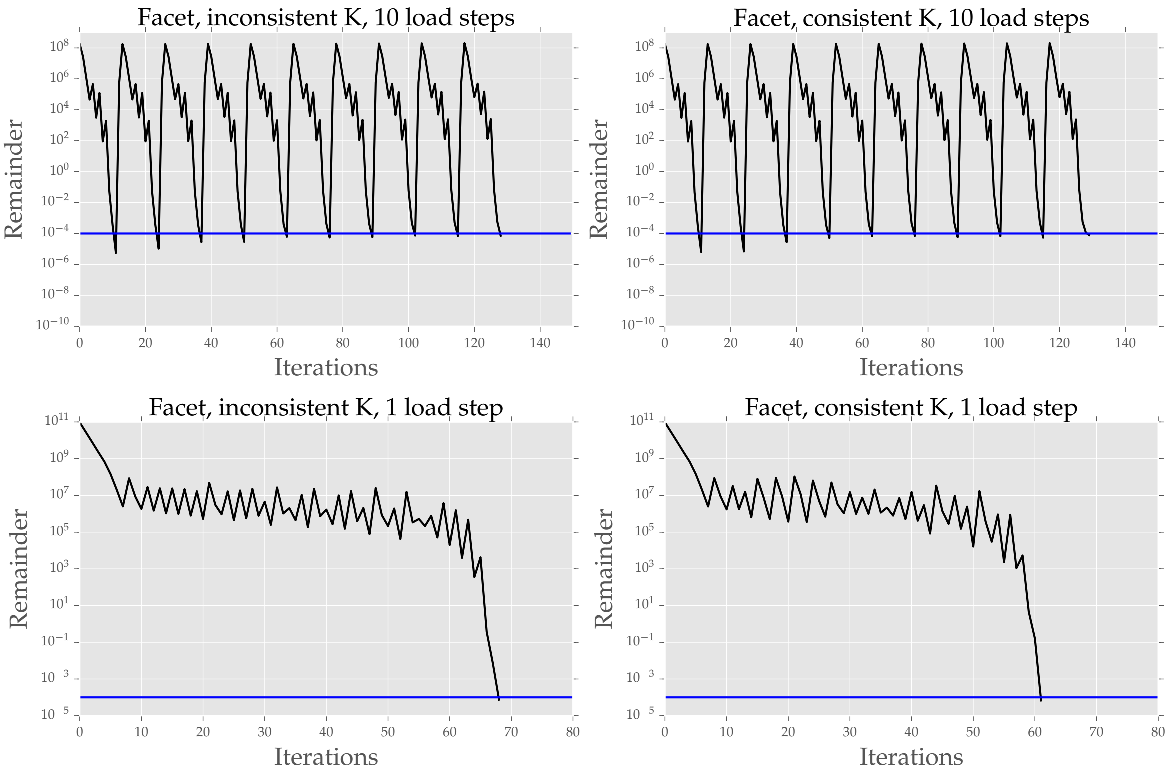

Figure E.3: Force remainder for bending of a strip simulation

Hemispherical shell

A hemispherical shell is tested with a 18^{o} top hole. The Young's modulus is $E = 8.625 \cdot 10^{7}$, the Poisson's ratio $v = 0.3$, the radius $R = 10$ and the thickness $h = 0.04$. A quadrant is simulated with load case and mesh shown in Figure E.5.

The deflections of the tips which were loaded are plotted compared to the applied load. A load of $150\ [N]$ is applied in 15 load steps. A force convergence criteria is used with a force norm tolerance of $1 \cdot 10^{-5}$.

Hinged cylindrical roof under concentrated load

Finally the results of the Cylindrical roof test are presented. This problem is ideal to test the non-linear solution procedure because the problem exhibits snap-back behaviour. We use the arc-length method by [57]. The simulation is compared with results from [71]. The thesis from Schellekens [72] gives

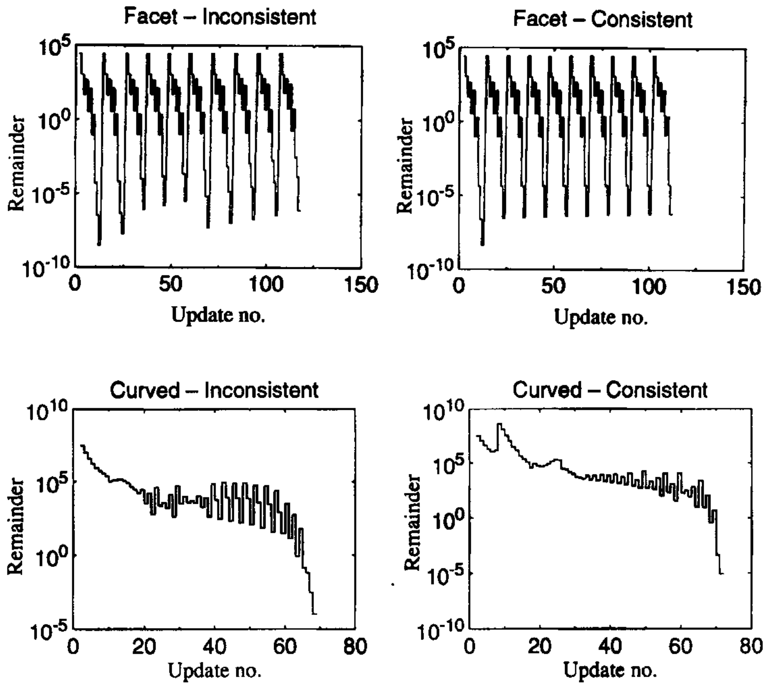

Figure E.4: Force remainders from Bout and van Keulen [54] for bending of a strip

more backround information on the problem.

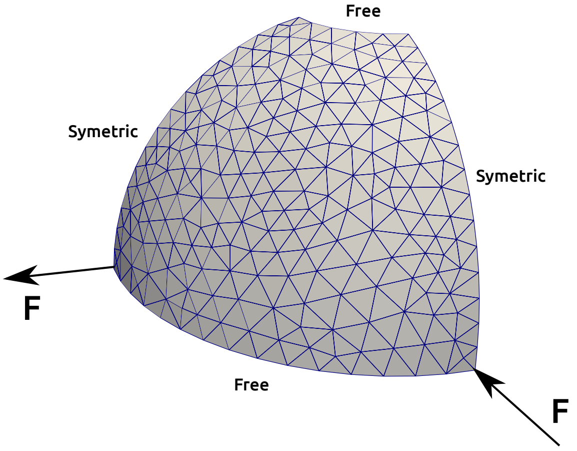
Free
Symetric
Symetric
F
Free
F

Figure E.5: Hemispherical shell, mesh, load case and boundary conditions

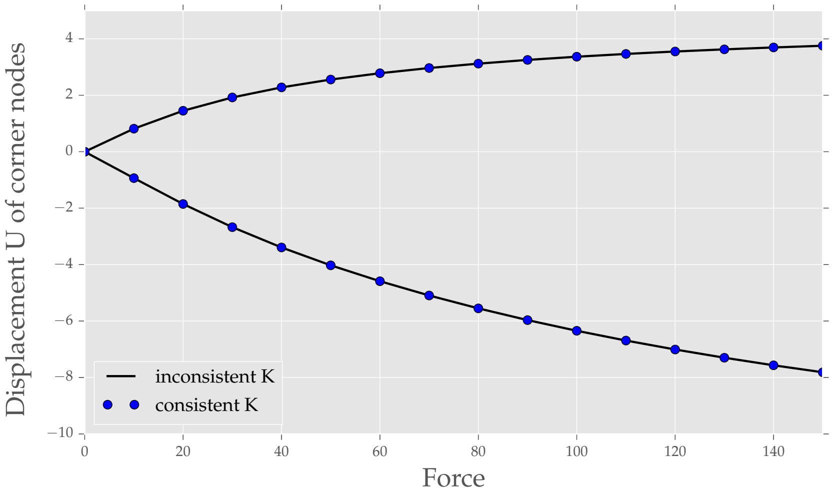

Figure E.6: Tip displacements of hemispherical shell

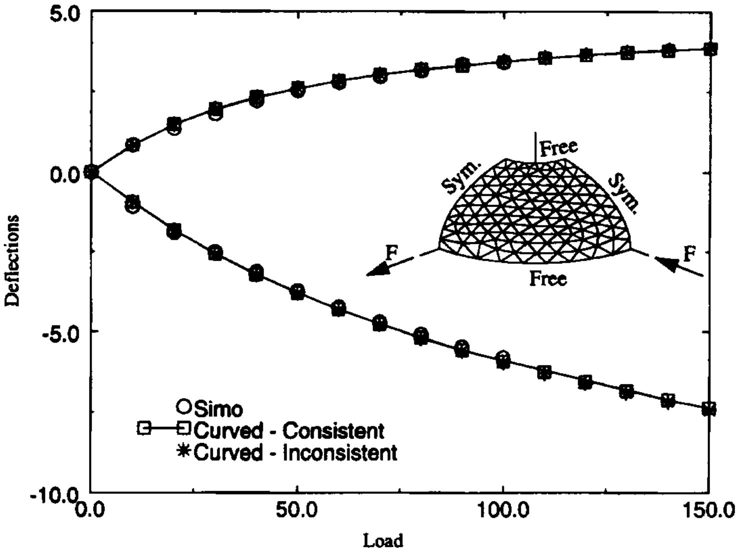

Figure E.7: Tip displacements of hemispherical shell from Bout and van Keulen [54]

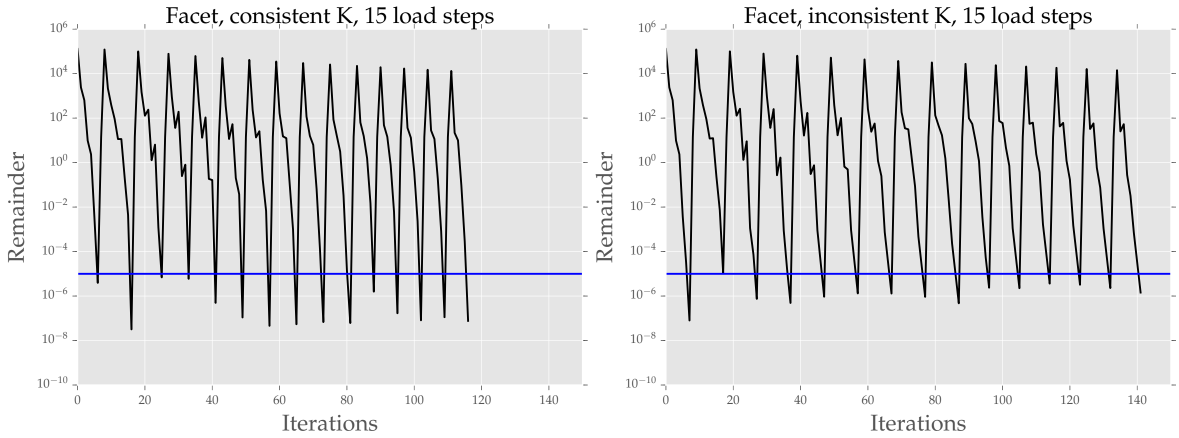

Figure E.8: Force remainder of hemispherical shell

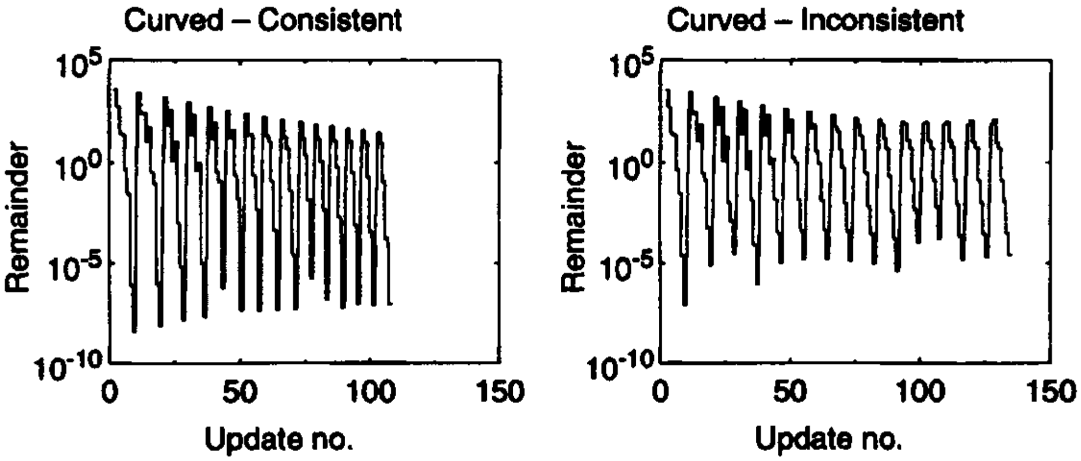

Figure E.9: Force remainder of hemispherical shell from Bout and van Keulen [54]

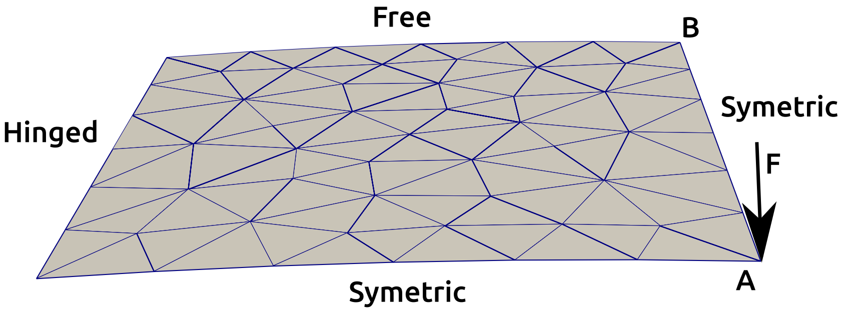
Free
B
Hinged
Symetric
F
Symetric
A

Figure E.10: Schematic of Cylindrical roof problem

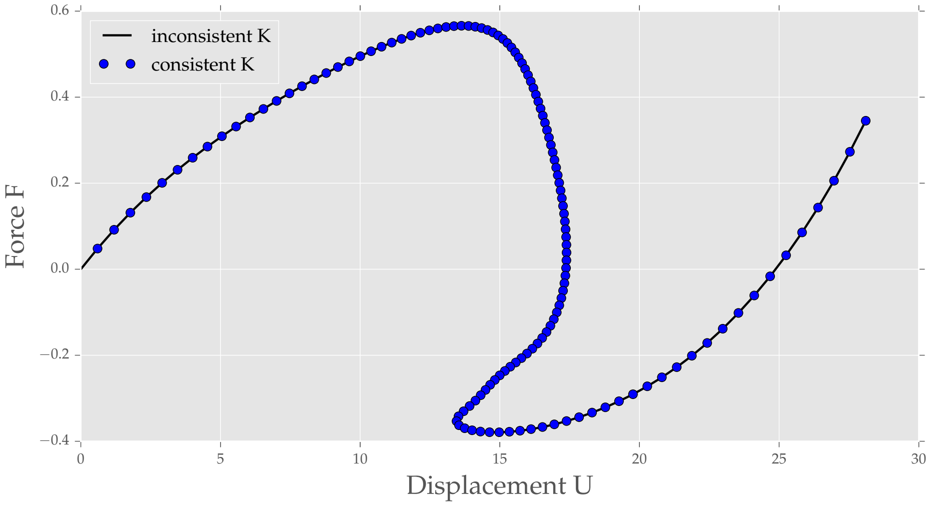

Figure E.11: Force-displacement graph for Cylindrical roof problem

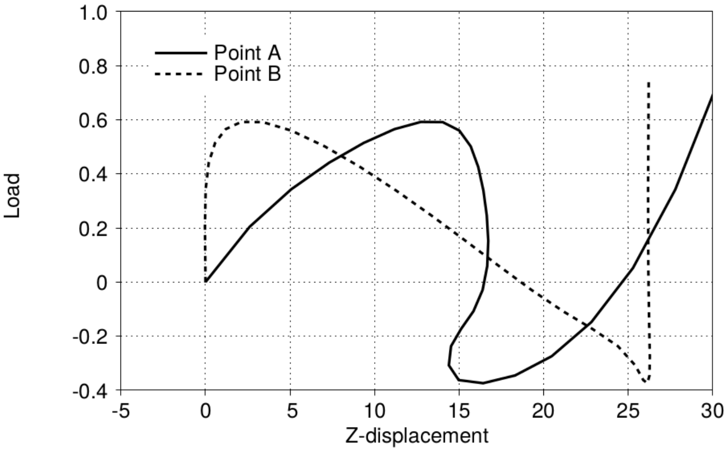

Figure E.12: Load-displacement graph of Cylindrical roof problem from [71]

F

Hinge connection element

In this appendix the Hinge connection element is discussed. The Hinge element can connect two shell elements along a side. The connection is an idealization, best illustrated by a door hinge. This means that for the translations, the elements are connected rigidly, but that the elements can rotate relative to each other controlled by a torsional stiffness k. In Figure F.1 the Hinge element is illustrated. Note that the orientation of the rotational DOF in the Figure are defined in a local coordinate system with regard to the Hinge element. The value of the rotational DOFs corresponding to the hinge sides is zero in the initial configuration.

The derivation of the stiffness matrix contribution of the Hinge element is described here. The internal virtual work due to the hinge δW_{hinge} is composed of σ and $\delta\phi$ which are work conjugates

$$\delta W_{hinge} = T\,\delta\phi.$$

with T, the torque composed of a material dependent parameter $k\;[Nm\,rad^{-1}]$ and a strain parameter ϕ which is written in terms of the rotational DOF of both hinge sides

$$T = k\,\delta\phi.$$

$$\phi = \varphi_1 - \varphi_2.$$

Substituting the above in the virtual work expression gives

$$\delta W_{hinge} = \phi^T\,k\,\delta\phi.$$

In matrix form this results in

$$\delta W_{hinge} = \begin{bmatrix} \delta\phi_1 & \delta\phi_2 \end{bmatrix} \begin{bmatrix} 1 \\ -1 \end{bmatrix} k \begin{bmatrix} 1 & -1 \end{bmatrix} \begin{bmatrix} \phi_1 \\ \phi_2 \end{bmatrix}.$$

This results in the contribution to the stiffness matrix

$$k \begin{bmatrix} 1 & -1 \\ -1 & 1 \end{bmatrix} \begin{bmatrix} \phi_1 \\ \phi_2 \end{bmatrix}.$$

The contribution to the internal forces is calculated by $F_{int} = \frac{\partial \Pi}{\partial \phi}$

$$\Pi[\phi] = \frac{1}{2}\,k\,(\varphi_1 - \varphi_2)^2$$

$$\frac{\partial \Pi}{\partial \varphi_1} = k(\varphi_1 - \varphi_2)$$

$$\frac{\partial \Pi}{\partial \varphi_2} = -k(\varphi_1 - \varphi_2).$$

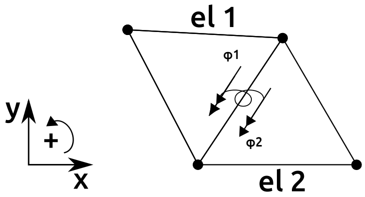
el 1
φ1
y
+
φ2
x
el 2

Figure F.1: Definition of the Hinge element

G

Periodic boundary conditions for finite rotation shell elements

Periodic Boundary Conditions (PBC) are boundary conditions which can be used in modeling a large system which is build up out off repeating building blocks. These building blocks are called Representative Volume Elements (RVE) and can usually be identified by observing a symmetry in the structure and shape of the deformation. By using only the RVE in the simulation and applying PBC correctly, computational time can be saved and the response of a RVE within the full system can be evaluated properly [73]. This section will investigate how to apply PBC in combination with the finite rotation shell element. A simple example problem is sought to investigate the effect of PBC on the translational- and rotational DOF of the shell element. A simple sine shaped strip is studied. If we observe the displacements at the periodic boundaries (two end points) of the strip during deformation we can imagine both ends move towards the center of the strip, resulting in a non-displacing center point $\mathbf{u}_c = \mathbf{0}$. Due to the symmetry of strip the two periodic boundaries should have opposite and equal horizontal displacements with respect to point c. Therefore, the displacements of the periodic boundary points are related through $u_x(1) = -u_x(2)$. The same reasoning was used by Danielsson *et al.* [73].

For shell type periodic problems rotational DOF are present at the periodic boundaries. For the rotations in the PBC we are concerned about the continuity of the structure. To fulfill continuity requirement of the structure, the rotational DOF and curvature (bending strain) at the periodic boundaries should be equal. For the sine strip example holds $\varphi(1) = \varphi(2)$ and $\chi_x(1) = -\chi_x(2)$. The first requirement can easily be satisfied but the curvature is depending on the rotational DOF φ_i and the updating of the reference vector $\mathbf{r}_i$. The updating of the reference vector is influenced by the directional change of the corresponding side vector. This means that the continuity requirements are met by using the rotational DOF only if the reference vectors do not change direction. Observing a sine strip example we see that the position of the sides can differ from the undeformed configuration s_1 and s_2 to the deformed configuration s_1' and s_2' but the direction of the sides stay identical. This is characteristic for several RVE in shell type periodic problem. Another periodic shell problem can be constructed where the periodic sides does change direction. This is a more complex case to analyze. An example of a more challenging case is the Miuri-ori sheet where we assume the faces are deformed by a finite stiffness of the fold lines. We observed that the side vectors at the periodic boundaries undergo an identical directional change and therefore we can apply periodic rotations at the rotational DOF. If other examples are found were the directional change of the side vectors is different, probably another RVE can be defined were the side vectors does change identical.

We conclude that for the translations and rotations the PBC can be implemented using a master-slave principle where the displacements and rotations of the periodic boundaries are related by a function depending on the problem. The assumption is that the direction of the periodic boundary sides do not change or that the change is identical, which is characteristic for several shell type periodic problems.

Bibliography

[1] K. Hatori, *History of Origami in the East and the West before Interfusion,* Origami 5: Fifth International Meeting of Origami Science, Mathematics, and Education , 3 (2011).

[2] A. Rafsanjani and K. Bertoldi, *Buckling-Induced Kirigami,* Physical Review Letters **084301** (2017), 10.1103/PhysRevLett.118.084301, arXiv:1702.06470 .

[3] A. Rafsanjani and D. Pasini, *Bistable auxetic mechanical metamaterials inspired by ancient geometric motifs,* Extreme Mechanics Letters **9**, 291 (2016), arXiv:1612.05988 .

[4] L. H. Dudte, E. Vouga, T. Tachi, and L. Mahadevan, *Programming curvature using origami tessellations,* Nature Materials **15**, 583 (2016).

[5] C. Lv, D. Krishnaraju, G. Konjevod, H. Yu, and H. Jiang, *Origami based Mechanical Metamaterials.* Scientific reports **4**, 5979 (2014).

[6] D. a. McAdams and W. Li, *A Novel Method to Design and Optimize Flat-Foldable Origami Structures Through a Genetic Algorithm,* Journal of Computing and Information Science in Engineering **14**, 031008 (2014).

[7] E. A. Peraza Hernandez, D. J. Hartl, E. Akleman, and D. C. Lagoudas, *Modeling and analysis of origami structures with smooth folds,* CAD Computer Aided Design **78**, 93 (2016).

[8] S. A. Zirbel, R. J. Lang, M. W. Thomson, D. A. Sigel, P. E. Walkemeyer, B. P. Trease, S. P. Magleby, and L. L. Howell, *Accommodating thickness in origami-based deployable arrays,* Journal of Mechanical Design **135**, 111005 (2013).

[9] C. Cromvik, *Numerical Folding of Airbags Based on Optimization and Origami,* Licentiate Thesis, Department of Mathematics, Chalmers University of Technology and Göteborg University, Sweden (2007).

[10] A. P. Thrall and C. P. Quaglia, *Accordion shelters: A historical review of origami-like deployable shelters developed by the US military,* Engineering Structures **59**, 686 (2014).

[11] K. Yang, S. Xu, J. Shen, S. Zhou, and Y. M. Xie, *Energy absorption of thin-walled tubes with prefolded origami patterns: Numerical simulation and experimental verification,* Thin-Walled Structures **103**, 33 (2016).

[12] K. Kuribayashi, K. Tsuchiya, Z. You, D. Tomus, M. Umemoto, T. Ito, and M. Sasaki, *Self-deployable origami stent grafts as a biomedical application of Ni-rich TiNi shape memory alloy foil,* Materials Science and Engineering A **419**, 131 (2006).

[13] C. D. Santangelo, *Extreme Mechanics: Self-Folding Origami,* Annual Review of Condensed Matter Physics **8**, annurev (2017).

[14] M. D. D. Ying Liu, Julie K. Boyles, Jan Genzer, *Self-folding of polymer sheets using local light absorption,* **8** (2012), 10.1039/c1sm06564e.

[15] K. C. Francis, J. E. Blanch, S. P. Magleby, and L. L. Howell, *Origami-like creases in sheet materials for compliant mechanism design,* , 371 (2013).

[16] H. C. Greenberg, M. L. Gong, S. P. Magleby, and L. L. Howell, *Identifying links between origami and compliant mechanisms,* , 217 (2011).

[17] J. Rommers, *Modeling and design of origami mechanisms with compliant facets,* (2015).

[18] H. Zimmer, M. Campen, D. Bommes, and L. Kobbelt, *Rationalization of Triangle-Based Point-Folding Structures,* **31** (2012), 10.1111/j.1467-8659.2012.03040.x.

[19] J. T. Overvelde, T. A. de Jong, Y. Shevchenko, S. A. Becerra, G. M. Whitesides, J. C. Weaver, C. Hoberman, and K. Bertoldi, *A three-dimensional actuated origami-inspired transformable metamaterial with multiple degrees of freedom,* Nature Communications **7**, 10929 (2016), arXiv:arXiv:1011.1669v3 .

[20] B. Florijn, C. Coulais, and M. Van Hecke, *Programmable mechanical metamaterials,* Physical Review Letters **113**, 2 (2014), arXiv:1407.4273 .

[21] E. Boatti, N. Vasios, and K. Bertoldi, *Origami Metamaterials for Tunable Thermal Expansion,* **1700360** (2017), 10.1002/adma.201700360.

[22] A. Reid, F. Lechenault, S. Rica, and M. Adda-Bedia, *Geometry and design of origami bellows with tunable response,* **013002**, 1 (2016), arXiv:1609.01354 .

[23] B. G. G. Chen, B. Liu, A. A. Evans, J. Paulose, I. Cohen, V. Vitelli, and C. D. Santangelo, *Topological Mechanics of Origami and Kirigami,* Physical Review Letters **116**, 1 (2016), arXiv:1508.00795 .

[24] N. Yang and J. L. Silverberg, *Decoupling local mechanics from large-scale structure in modular metamaterials,* (2017), 10.1073/pnas.1620714114.

[25] S. Waitukaitis, R. Menaut, B. G. G. Chen, and M. Van Hecke, *Origami multistability: From single vertices to metasheets,* Physical Review Letters **114**, 2 (2015), arXiv:1408.1607 .

[26] D. Restrepo, N. D. Mankame, and P. D. Zavattieri, *Phase transforming cellular materials,* Extreme Mechanics Letters **4**, 52 (2015).

[27] B. H. Hanna, J. M. Lund, R. J. Lang, S. P. Magleby, and L. L. Howell, *Waterbomb base: a symmetric single-vertex bistable origami mechanism,* Smart Materials and Structures **23**, 094009 (2014).

[28] B. H. Hanna, S. P. Magleby, R. J. Lang, and L. L. Howell, *Force–Deflection Modeling for Generalized Origami Waterbomb-Base Mechanisms,* **82**, 1 (2017).

[29] V. Brunck, F. Lechenault, A. Reid, and M. Adda-Bedia, *Elastic theory of origami-based metamaterials,* Physical Review E - Statistical, Nonlinear, and Soft Matter Physics **93**, 1 (2016).

[30] Z. Y. Weina Wu, *Modelling rigid origami with quaternions and dual quaternions,* **466**, 2155 (2010).

[31] Y. Chen, R. Peng, and Z. You, *Origami of thick panels,* , 1 (2015).

[32] Resch, *Kinematic folded plate systems,* (1971).

[33] M. Schenk, *Folded Shell Structures,* (2011).

[34] M. Schenk, S. D. Guest, U. C. Geometry, and F. S. Structures, *Geometry of Miura-folded metamaterials,* **110**, 3276 (2013).

[35] M. A. E. Kshad and H. E. Naguib, *Development and modeling of multi-phase polymeric origami inspired architecture by using pre-molded geometrical features,* **025012**.

[36] W. Gilewski and P. Stawarz, *Wojciech Gilewski,* **91**, 220 (2014).

[37] A. Gisario, M. Mehrpouya, S. Venettacci, A. Mohammadzadeh, and M. Barletta, *LaserOrigami (LO) of three-dimensional (3D) components: Experimental analysis and numerical modelling,* Journal of Manufacturing Processes **23**, 242 (2016).

[38] C. Jianguo, D. Xiaowei, Z. Ya, F. Jian, and T. Tongming, *Bistable behavior of the cylindrical origami structure with Kresling pattern,* Journal of Mechanical Design **137**, 061406 (2015).

[39] N. Wonoto, D. Baerlecken, R. Gentry, and M. Swarts, *Parametric Design and Structural Analysis of Deployable Origami Tessellation,* **4360** (2017), 10.3722/cadaps.2013.939-951.

[40] Adrienne Crivaro, *Modeling and validation of a compliant bistable mechanism acutated by magneto active elastomers,* (2014).

[41] W. Hamouche, C. Maurini, A. Vincenti, and S. Vidoli, *Basic criteria to design and produce multi-stable shells,* Meccanica **51**, 2305 (2016).

[42] J. L. Silverberg, J.-H. Na, A. A. Evans, B. Liu, T. C. Hull, C. D. Santangelo, R. J. Lang, R. C. Hayward, and I. Cohen, *Origami structures with a critical transition to bistability arising from hidden degrees of freedom.* Nature materials **14**, 389 (2015).

[43] H. Yasuda, Z. Chen, and J. Yang, *Multitransformable Leaf-Out Origami With Bistable Behavior,* **8**, 4 (2017).

[44] J. M. Gattas, W. Lv, and Y. Chen, *Rigid-foldable tubular arches,* Engineering Structures **145**, 246 (2017).

[45] M. Wardetzky, E. Vouga, and O. Gottesman, *On the Incompressibility of Cylindrical Origami Patterns,* **139**, 1 (2017).

[46] S. Li and K. W. Wang, *Fluidic origami with embedded pressure dependent multi-stability: a plant inspired innovation,* (2015).

[47] S. Li, H. Fang, and K. W. Wang, *Recoverable and Programmable Collapse from Folding Pressurized Origami Cellular Solids 1,* **c**, 1 (2016).

[48] H. Yasuda and J. Yang, *Reentrant origami-based metamaterials with negative Poisson's ratio and bistability,* Physical Review Letters **114**, 1 (2015).

[49] A. Bovier, *Metastability* (Springer, 2015) p. 578.

[50] T. Frenzel, C. Findeisen, M. Kadic, P. Gumbsch, and M. Wegener, *Tailored Buckling Microlattices as Reusable Light-Weight Shock Absorbers,* Advanced Materials , 5865 (2016).

[51] S. Shan, S. H. Kang, J. R. Raney, P. Wang, L. Fang, F. Candido, J. A. Lewis, and K. Bertoldi, *Multistable Architected Materials for Trapping Elastic Strain Energy,* Advanced Materials **27**, 4296 (2015), arXiv:1207.1956 .

[52] E. J. Mittemeijer, *Fundamentals of Materials Science* (Springer, 2010).

[53] F. Van Keulen, *On refined triangular plate and shell elements,* (1993).

[54] J. Booij and F. Van Keulen, *Refined consistent formulation of a curved triangular finite rotation shell element,* **39**, 2803 (1996).

[55] B. K. Donaldson, *Introduction to Structural Dynamics*.

[56] C. L. D. Philip D. Cha, James J. Rosenberg, *Fundamentals of Modeling and Analyzing Engineering Systems* (2000).

[57] S. E. Leon, G. H. Paulino, A. Pereira, I. F. M. Menezes, and E. N. Lages, *A Unified Library of Nonlinear Solution Schemes,* Applied Mechanics Reviews **64**, 040803 (2011).

[58] B. Holtzer, *Topology Optimization of Geometrically Nonlinear Structures*, Ph.D. thesis (2017).

[59] T. Grätsch, K.-J. K.-J. Bathe, T. Gratsch, and K.-J. K.-J. Bathe, *A posteriori error estimation techniques in practical finite element analysis,* Computers Structures **83**, 235 (2005).

[60] T. Grätsch and K.-J. Bathe, *Influence functions and goal-oriented error estimation for finite element analysis of shell structures,* International Journal for Numerical Methods in Engineering **63**, 709 (2005).

[61] A. documentation, *Abaqus Theory Manual,* (2017).

[62] J. T. B. Overvelde, J. C. Weaver, C. Hoberman, and K. Bertoldi, *Rational design of reconfigurable prismatic architected materials,* Nature **541**, 347 (2017).

[63] D. Morley, *The constant-moment plate-bending element,* (1971).

[64] Colorado University, *Variational Formulation of Plane Beam Element,* (2016).

[65] T. H. H. Pian, *State-of-the-art development of hybrid/mixed finite element method,* Finite Elements in Analysis and Design **21**, 5 (1995).

[66] T. H. H. Pian, *A historical note about 'hybrid elements',* International Journal for Numerical Methods in Engineering **12**, 891 (1978).

[67] Colorado University, *The Bernoulli-Euler Beam,* (2016).

[68] E. Byskov, *Elementary Continuum Mechanics* (Springer, Aalborg, 2013).

[69] Colorado University, *Kirchhoff Plates: Field Equations,* (2016).

[70] Colorado University, *Three-Node Plane Stress Triangles,* (2016).

[71] Colorado University, *Numerical Examples of Thin Shell Analysis,* (2016).

[72] J. Schellekens, *Computational strategies for composite structures,* (1992).

[73] M. Danielsson, D. M. Parks, and M. C. Boyce, *Three-dimensional micromechanical modeling of voided polymeric materials,* Journal of the Mechanics and Physics of Solids **50**, 351 (2002).